Torsional Vibration in the National Wind Technology Center's 2.5-Megawatt Dynamometer

Latha Sethuraman, Jonathan Keller, and Robb Wallen
National Renewable Energy Laboratory

NREL is a national laboratory of the U.S. Department of Energy
Office of Energy Efficiency & Renewable Energy
Operated by the Alliance for Sustainable Energy, LLC

This report is available at no cost from the National Renewable Energy Laboratory (NREL) at www.nrel.gov/publications.

Technical Report
NREL/TP-5000-65658
August 2016

Contract No. DE-AC36-08GO28308

NREL
NATIONAL RENEWABLE ENERGY LABORATORY

Torsional Vibration in the National Wind Technology Center's 2.5-Megawatt Dynamometer

Latha Sethuraman, Jonathan Keller, and Robb Wallen
National Renewable Energy Laboratory

Prepared under Task No. WE15.4A04

NREL is a national laboratory of the U.S. Department of Energy
Office of Energy Efficiency & Renewable Energy
Operated by the Alliance for Sustainable Energy, LLC

This report is available at no cost from the National Renewable Energy Laboratory (NREL) at www.nrel.gov/publications.

National Renewable Energy Laboratory
15013 Denver West Parkway
Golden, CO 80401
303-275-3000 • www.nrel.gov

Technical Report
NREL/TP-5000-65658
August 2016

Contract No. DE-AC36-08GO28308

This report is available at no cost from the National Renewable Energy Laboratory (NREL) at www.nrel.gov/publications.

Available electronically at SciTech Connect http:/www.osti.gov/scitech

Available for a processing fee to U.S. Department of Energy and its contractors, in paper, from:

U.S. Department of Energy
Office of Scientific and Technical Information
P.O. Box 62
Oak Ridge, TN 37831-0062
OSTI http://www.osti.gov
Phone: 865.576.8401
Fax: 865.576.5728
Email: reports@osti.gov

Available for sale to the public, in paper, from:

U.S. Department of Commerce
National Technical Information Service
5301 Shawnee Road
Alexandria, VA 22312
NTIS http://www.ntis.gov
Phone: 800.553.6847 or 703.605.6000
Fax: 703.605.6900
Email: orders@ntis.gov

Cover Photos by Dennis Schroeder: (left to right) NREL 26173, NREL 18302, NREL 19758, NREL 29642, NREL 19795.

NREL prints on paper that contains recycled content.

Acknowledgments

This work was supported by the U.S. Department of Energy under contract with the National Renewable Energy Laboratory. Funding for the work was provided by the DOE Office of Energy Efficiency and Renewable Energy, Wind and Water Power Technologies Office.

List of Acronyms

DGB	dynamometer gearbox
GB	gearbox
HSS	high-speed shaft
Hz	hertz
kg	kilogram
kN	kilonewton
kNm	kilonewton-meter
kW	kilowatt
LPF	low-pass filter
LSS	low-speed shaft
m	meter
MW	megawatt
NREL	National Renewable Energy Laboratory
NWTC	National Wind Technology Center
PMSM	permanent-magnet synchronous machine
rpm	revolutions per minute

Table of Contents

List of Figures

List of Tables

1 Introduction

The National Wind Technology Center's (NWTC's) 2.5-megawatt (MW) dynamometer is a state-of-the art test facility within the National Renewable Energy Laboratory (NREL) dedicated to testing and performance validation of drivetrains in a controlled environment [1]. Since 2000, the test facility has been part of several successful test campaigns that have enabled original equipment manufacturers to address drivetrain design issues related to operation, reliability, control, and safety prior to full-scale field testing and commercialization. The dynamometer is able to simulate different operating regimes, allowing both static and dynamic testing of fully integrated drivetrain systems including gearboxes, generators, and power electronic converters.

A recent test campaign involving a test article drive-train [2] revealed the excitation of a torsional mode in the dynamometer that made testing impractical at higher load levels, encouraging a detailed investigation into the sources and causes of such excitation. The 2.5-MW dynamometer is equipped with a large motor and gearbox, which, when coupled to a test article drivetrain, can introduce several potential sources of compliance along the torque load-path; hence, system torsional natural frequencies must be identified to avoid excitations.

This report documents the torsional drivetrain dynamics of the NWTC's 2.5-MW dynamometer as identified experimentally and as calculated using lumped parameter models [3] using known inertia and stiffness parameters. The report is presented in two parts beginning with the identification of the primary torsional modes followed by the investigation of approaches to damp the torsional vibrations. The key mechanical parameters for the lumped parameter models and justification for the element grouping used in the derivation of the torsional modes are presented. The sensitivities of the torsional modes to different test article properties are discussed.

The oscillations observed from the low-speed and generator torque measurements were used to identify the extent of damping inherently achieved through active and passive compensation techniques. A simplified Simulink model of the dynamometer test article integrating the electro-mechanical power conversion and control features was established to emulate the torque behavior that was observed during testing. The torque response in the high-speed, low-speed, and generator shafts were tested and validated against experimental measurements involving step changes in load with the dynamometer operating under speed-regulation mode. The Simulink model serves as a ready reference to identify the torque sensitivities to various system parameters and to explore opportunities to improve torsional damping under different conditions.

2 Dynamometer and Test Article Description

The NWTC 2.5-MW dynamometer (Figure 1) is powered by a three-phase AC induction motor rated at 3,351 HP 4,160 V, 415 A. The motor is controlled by a variable frequency drive with full regeneration capacity [4]. The motor is connected to a three-stage reduction gearbox through a high-speed flexible coupling. In addition, a torque limiter (Voith safeset SRP-150 [5]) between the coupling and the gearbox acts as a safety mechanism, interrupting the power flow in the driveline in the event of excessive operational loads. The gearbox has a speed reduction ratio of 51.3832, which allows low operating speeds typically ranging from 0 to 44 revolutions per minute (rpm). Continuous torque of 1,000 kilonewton-meters (kNm) up to 22 rpm and continuous power of 2.5 MW up to 44 rpm are possible. A multichannel 24-bit distributed data acquisition system allows for data collection at both slower and faster sampling rates. The dynamometer can be operated in either torque control or speed control mode depending on the regulation capability available at the test article. In torque control mode, the operator commands a torque that the motor applies, and the test article drivetrain regulates the speed. In speed control mode, the operator commands the motor's speed, and torque is regulated by the test article drivetrain.

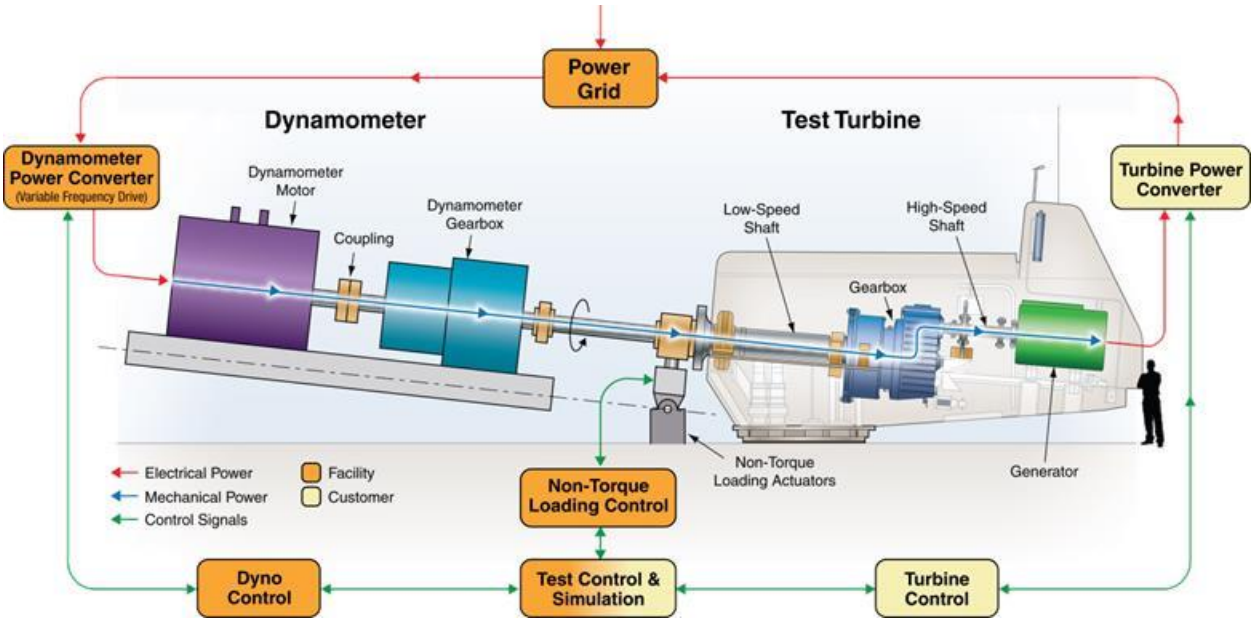

Figure 1. NWTC's 2.5-MW dynamometer. *Illustration by NREL* [4]

The test article under investigation in this case was the next-generation drivetrain [2]. It is rated for 750-kilowatt (kW) medium-speed operation with a single-stage planetary gearbox (speed ratio of 5.82). The drivetrain uses a permanent-magnet generator with a power electronic converter that can control generator torque to follow an approximate square law relative to speed. It was preferred to operate the dynamometer in speed-control mode because the test article generator did not have a speed-control loop.

The physical layout of the test article is shown in Figure 2. The main shaft of the test article (identified by item 6) is connected to the dynamometer shaft through a low speed coupling (identified by item 5) manufactured by Ameridrives [6, 7]. Table 1 lists the key mechanical properties of the dynamometer motor (1), gearbox (4), low-speed coupling and the test article

(items 6-9). All quantities are referred to the low-speed side of the dynamometer, taking the speed ratios of the dynamometer gearbox and test article into proper account. For more detailed description of the components and derivations of the stiffness properties, refer to Appendices A and B.

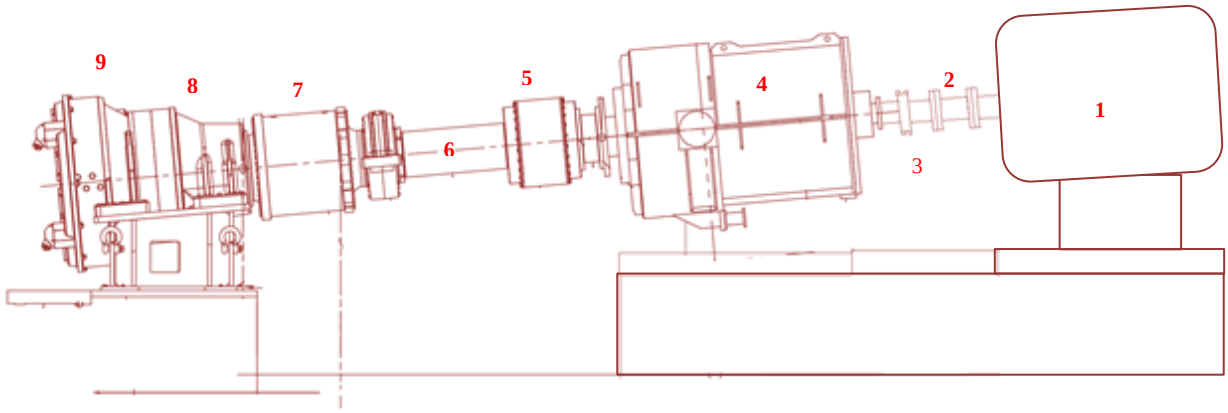

Figure 2. Dynamometer test assembly. ***Illustration reproduced from [8]***

A careful inspection of the component stiffnesses and the inertia properties reveals that the inertias of dynamometer motor (J_m), dynamometer gearbox (J_{DGB}), and the test article (J_{TA}) represented the three largest elements with the main sources of compliance along the torque path being the torque limiter (K_{tl}) and test article (K_{TA}). This information is helpful to identify the main elements(also highlighted in Table 1) that drive the torsional vibration modes of the drivetrain system and help formulate a suitable torsional equivalent lumped parameter model.

Table 1. Dynamometer and Test Article Properties

Item No.	Component	Symbol	Moment of Inertia (kg-m^2)	Symbol	Torsional Stiffness (Nm/rad)	Manufacturer/ Document Reference
1	Dynamometer motor	$\boldsymbol{J_m}$	649756	K_M	2.71E+10	Data sheet [9]
2	Flexible coupling (High speed)	$J_{HS\text{-}C}$	9735	$K_{HS\text{-}C}$	1.85E+10	Rexroth data sheet [10]
3	Torque limiter	J_{tl}	4868	$\boldsymbol{K_{tl}}$	5.07E+08	Voith SR_P150 [5]
4	Dynamometer gearbox	$\boldsymbol{J_{DGB}}$	150619	K_{dgb}	6.87E+08	MOD2 data sheet [11] ; APPENDIX-A
5	Flexible coupling(Low-speed)	$J_{LS\text{-}C}$	656.42	$K_{LS\text{-}C}$	1.71E+10	Ameridrives data sheet [6,7]
6-9	Test article drivetrain	$\boldsymbol{J_{TA}}$*	46144	$\boldsymbol{K_{TA}}$*	7.66E+07	Romax report [12]; APPENDIX-B
	Test article generator	J_G	41663	$\boldsymbol{K_G}$		

**Includes items 6 through 9; for detailed derivation of the inertias and stiffnesses, refer to Appendix B*

3 Torsional Modes

This section discusses the derivation of the torsional modes using the lumped parameter models and the experimental results used to validate the model. A few additional reduced order models together with their accuracy in representing the torsional modes are also presented. The sensitivities of the torsional modes to test article properties are explained.

3.1 Torsional Dynamic Equivalent of the Test Set-Up

The dynamometer and test article represent a complex multi-degree of freedom system; the inertias associated with the dynamometer motor, the gearbox, test article gearbox and generator in combination with the mechanical compliance or spring rates of the mechanical drivetrain, including the generator shaft, may create a distributed mechanical spring-mass system that exhibits torsional oscillations. Figure 3 shows a lumped three-mass equivalent representation of the drivetrain.

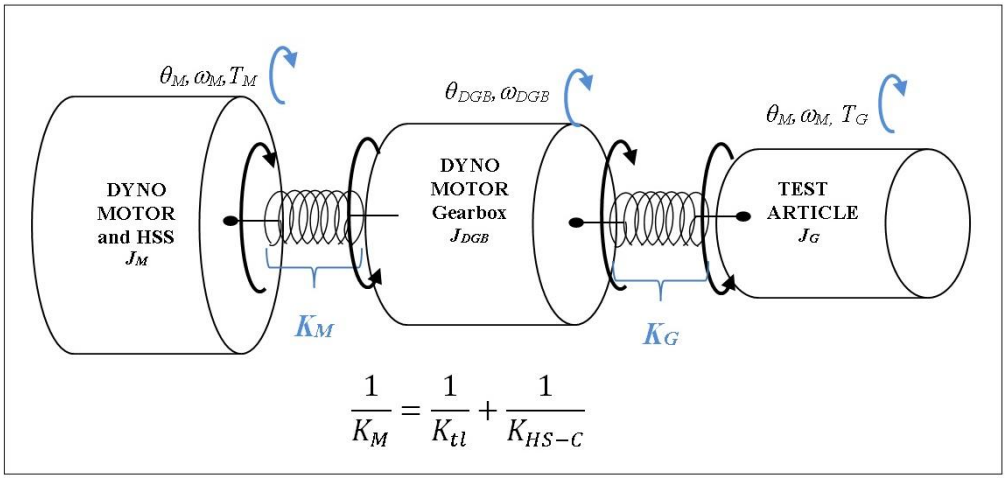

Figure 3. Torsional mass-spring equivalent of the 2.5-MW dynamometer

The elements lumped under J_M include the inertias of the dynamometer motor and the dyno high-speed shaft. The high-speed coupling and torque limiter form the first spring element, K_M. All the elements inside the dynamometer gearbox are grouped under J_{DGB}. The second spring element, K_G, includes the stiffnesses of the main shaft, low-speed coupling, adapter, test article gearbox, and generator rotor. The dynamometer torque and the generator reaction torque act in opposite sense. Three degrees of freedom define the independent coordinates required to describe the rotational motion of this vibratory system.

Let $\dot{\theta}_i, \omega_i$, and $\dot{\omega}_i$ (where i={*M*,*DGB*,*G*}) represent the position, velocity, and angular acceleration of the mass equivalents of the dynamometer motor, gearbox, and the test article, respectively. Torsional vibration can be determined using the dynamics equations for the three-mass model [3] as follows:

$$\begin{bmatrix} \dot{\omega_M} \\ \dot{\omega_{DGB}} \\ \dot{\omega_G} \\ \dot{\theta_M} \\ \dot{\theta_{DGB}} \\ \dot{\theta_G} \end{bmatrix} = \begin{bmatrix} -B_M/J_M & 0 & 0 & -K_M/J_M & K_M/J_M & 0 \\ 0 & -B_{DGB}/J_{NTL} & 0 & K_M/J_{DGB} & -(K_M+K_G)/J_{J_{DGB}} & K_G/J_{J_{DGB}} \\ 0 & 0 & -B_G/J_G & 0 & K_M/J_G & -K_M/J_G \\ 1 & 0 & 0 & 0 & 0 & 0 \\ 0 & 1 & 0 & 0 & 0 & 0 \\ 0 & 0 & 1 & 0 & 0 & 0 \end{bmatrix} \begin{bmatrix} \omega_M \\ \omega_{DGB} \\ \omega_G \\ \theta_M \\ \theta_{DGB} \\ \theta_G \end{bmatrix} + \begin{bmatrix} 1/J_M & 0 \\ 0 & 0 \\ 0 & 1/J_G \\ 0 & 0 \\ 0 & 0 \\ 0 & 0 \end{bmatrix} \begin{bmatrix} T_M \\ T_G \end{bmatrix} \quad (1)$$

where B_i and K_i (with i={*M,DGB,G*}) represent the damping and stiffness lumped between the three mass equivalents. The dynamometer and generator speed and angle are in the directions as defined in the figure. The eigenvalues of equation (1) are given by:

$$\begin{bmatrix} \lambda_1 \\ \lambda_2 \\ \lambda_3 \end{bmatrix} = \begin{bmatrix} 0 \\ \frac{-b+\sqrt{b^2-4ac}}{2a} \\ \frac{-b-\sqrt{b^2-4ac}}{2a} \end{bmatrix} \quad (2)$$

where

$$a = J_M \cdot J_{DGB} \cdot J_G \quad (3)$$

$$b = K_G J_G (J_M + J_{DGB}) + K_g J_M (J_{DGB} + J_G) \quad (4)$$

$$c = K_M \cdot K_G (J_M + J_{DGB} + J_G) \quad (5)$$

The mode shapes (X_i) are the nontrivial eigenvectors that satisfy the eigenvalue equation such that:

$$(M^{-1}K)X_i = \lambda_i X_i \text{ , where i =1, 2, 3} \quad (6)$$

The first eigenvalue, λ_1, results in a rigid body mode with all three masses oscillating in phase with each other (i.e., $\theta_M = \theta_{DGB} = \theta_G$). The torsional model parameters, when applied to equations (2) and (3), result in two remaining natural frequencies, 6.45 hertz (Hz) and 10.9 Hz, respectively. Table 2 lists the frequencies and mode shapes. The second mode shape corresponding to 6.45 Hz represents the case where both the dynamometer gearbox and the test article oscillate in phase with each other. The vibration amplitude at the motor is small, but is out of phase with both the gearbox and the test article. The third mode corresponding to 10.9 Hz represents the case where the motor and test article are in phase while the dynamometer gearbox moves out of phase.

Table 2. Frequencies and Mode Shapes (Three-Mass Model)

Mode	Frequency	Mode Shape
1	0	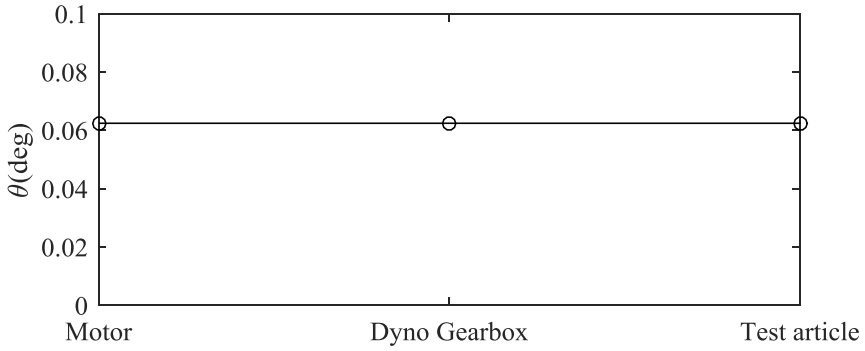
2	6.45 Hz	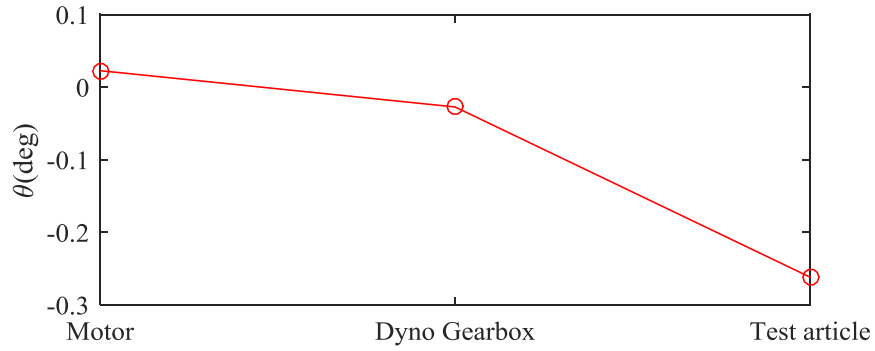
3	10.948 Hz	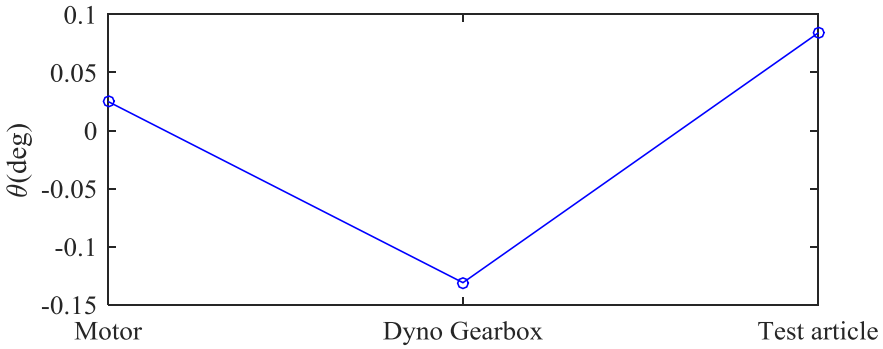

3.2 Measured Resonance under Torque Testing

A series of tests covering a range of torque and speed levels was carried out to ascertain the main excitation frequencies and also help identify the extent of damping achieved through active and passive compensation techniques. The intent of such measures was to avoid transient dynamics while allowing a smooth ramp-up in speed and torque during testing. Torsional resonance of the dynamometer was initially observed through measurements made during short-duration torque testing. Small steps in power/torque were applied at the dynamometer. The step-wise loading covered the torque span from 20 kNm up to 412 kNm while the speed ranged from 6 to 13 rpm. Torque measurements were made using strain gauges located on the low-speed side of the dynamometer and high-speed side of the test article. Speed and azimuth data were collected from an encoder positioned on the dynamometer motor (the speed on the low-speed shaft and the test article generator were inferred by applying transformation ratios). The data acquisition system measured generator torque and power.

Each load step application lasted for approximately 15-second (s) duration, and the measurements were sampled at 2,000 Hz. Each load step input was accompanied by large oscillations in torque at the low-speed shaft side with a range of ± 50 kNm. The generator torque also showed oscillations with a range of ±10 kNm, which were in phase with the dynamometer. The decay time for the oscillations between the dynamometer and generator torques increased with an increase in power levels. Figure 4 shows the sample time histories of torque measurements on the low-speed shaft and the generator.

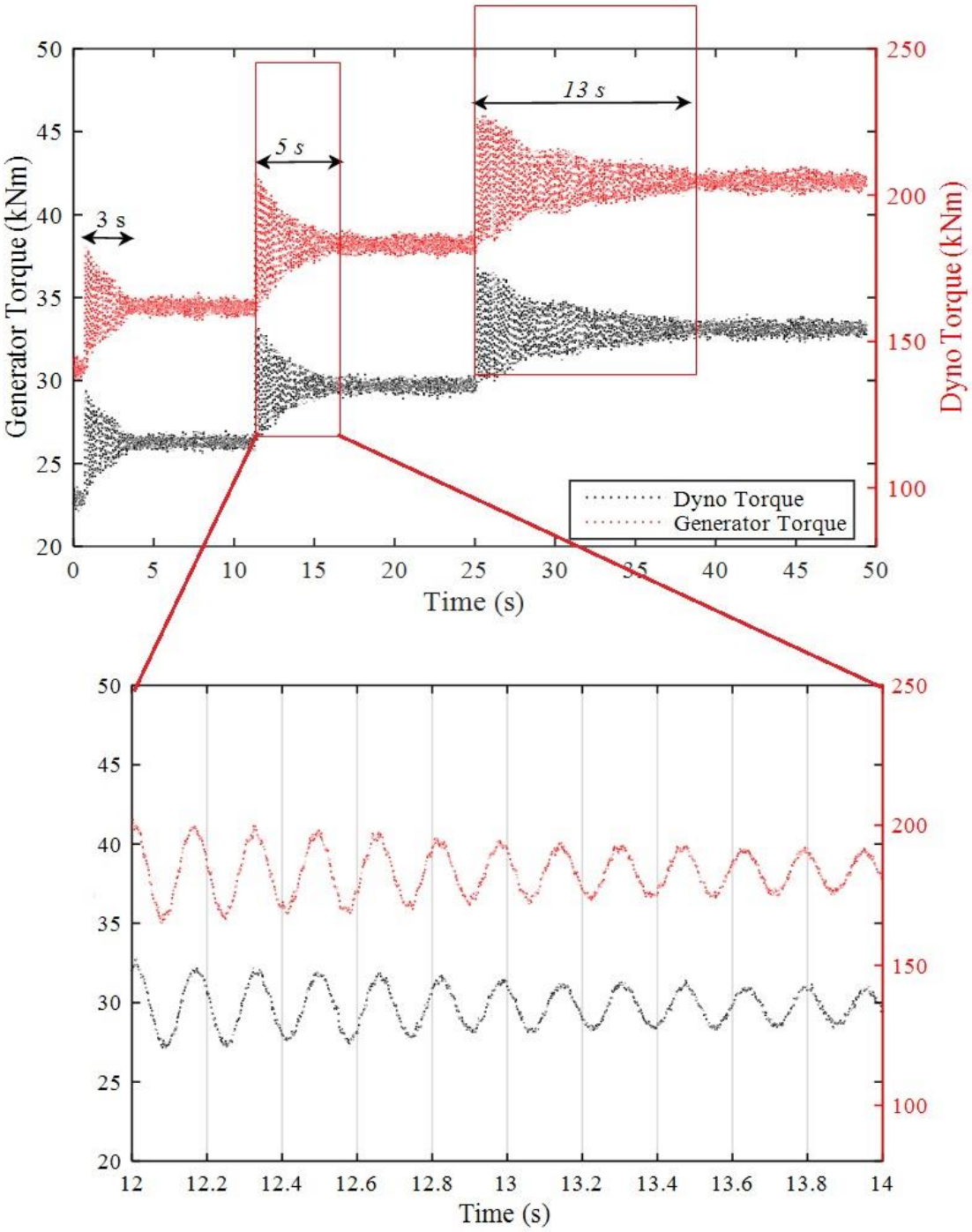

Figure 4. Torque measurements at the dynamometer low-speed shaft and test article generator

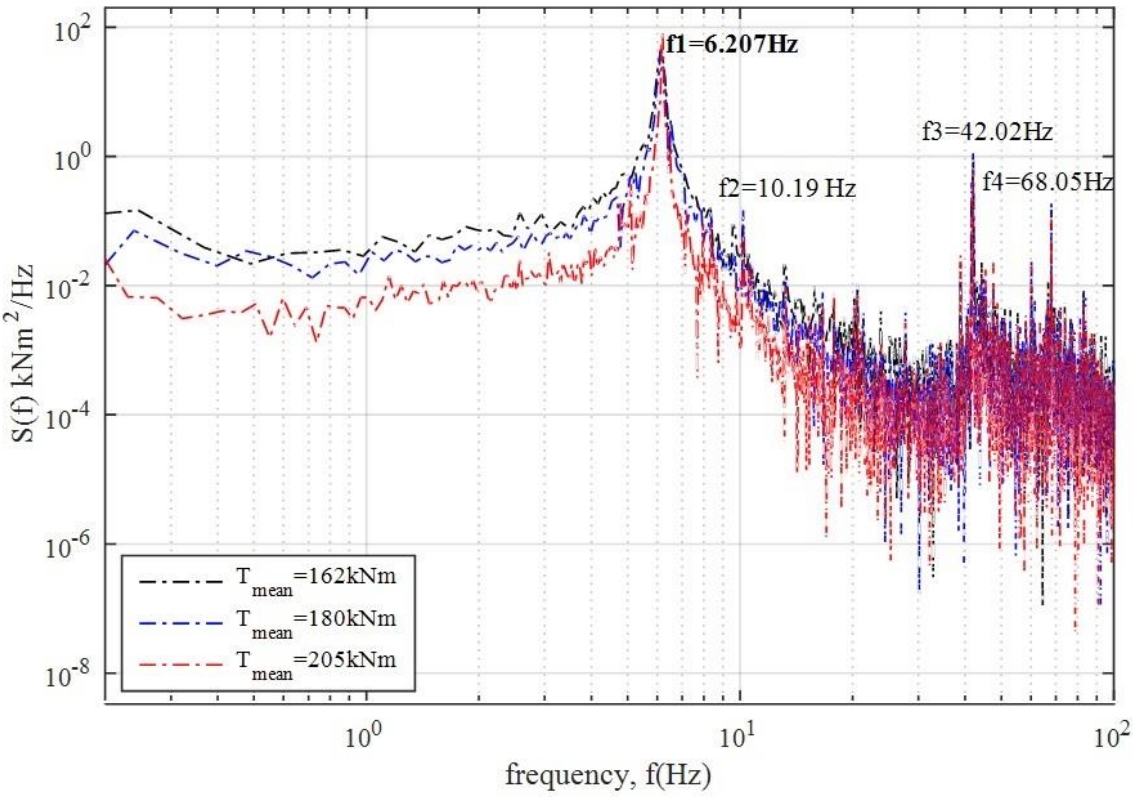

Figure 5. Frequency response of dynamometer torque

In Figure 5, four frequency peaks are identified from the frequency response of the dynamometer torque at 6.21 Hz, 10.19 Hz, 42.02 Hz, and 68.05 Hz. The generator torque response (Figure 6) also showed peaks at 6.11 Hz, 10.19 Hz, and 41.64 Hz, whereas the fourth most dominating frequency was higher, at 91.86 Hz.

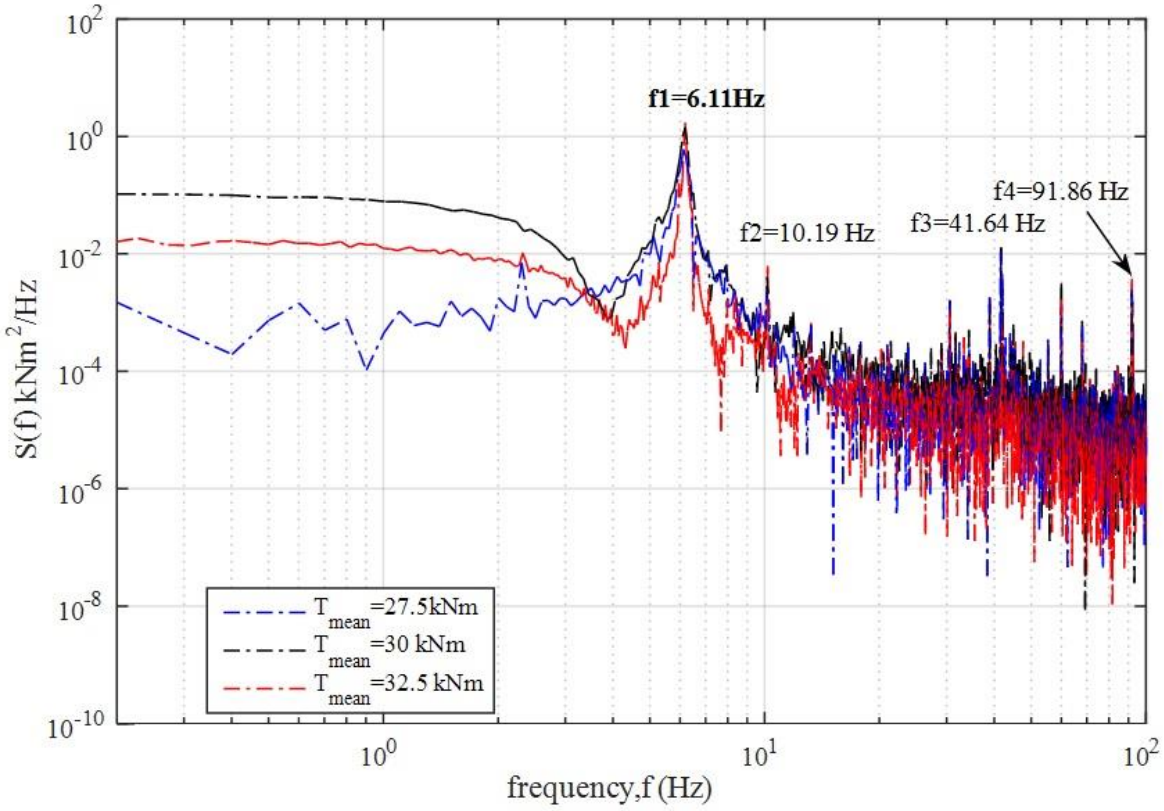

Figure 6. Frequency response of generator torque

In Figures 5 and 6, the first significant torsional mode identified by the three-mass lumped parameter model (6.5 Hz) closely matches with the dominant 6-Hz content observed in these torque measurements. Measurements also help identify the second torsional mode (10-Hz content) predicted by the lumped parameter model. The phase relationship between the two torques as noted in Figure 6 validates the second mode shape predicted by the model.

3.3 Stiffness Validation

A range of torque levels under controlled conditions was demanded from the dynamometer motor with the purpose of measuring the torsional wind-up of the dynamometer system. This was useful to empirically estimate the stiffness of the dynamometer as described in Section 4. A low-speed shaft (LSS) encoder was used to measure the shaft azimuth while the drivetrain was operating at different levels of torque (35 kNm–425 kNm). In all cases, the LSS data were acquired at 10 Hz for 1 second.

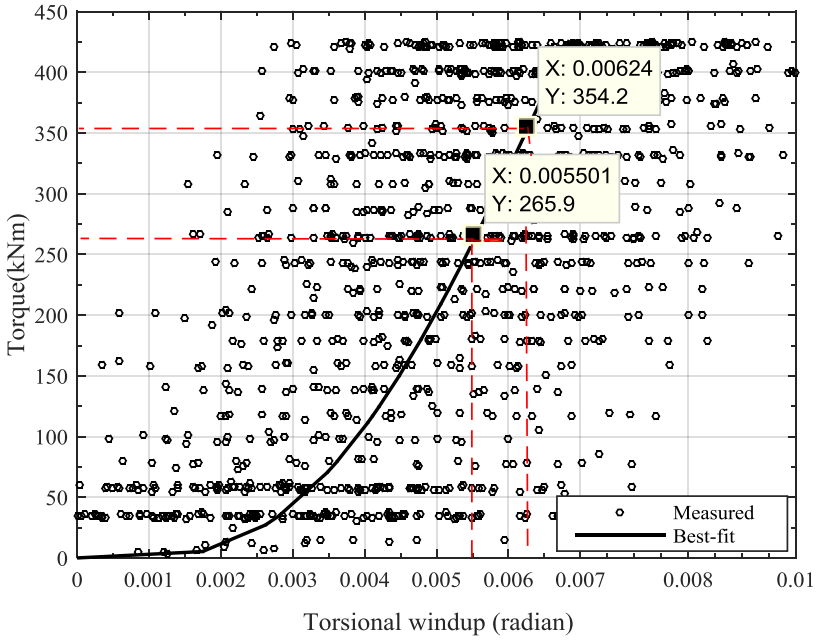

Figure 7. Torsional wind-up measurement

The measurement record showed a high degree of scatter, hence the extent of linearization or nonlinearity was indistinct; however, a moving average filter was applied to determine the best fit around the scatter. The slope of the curve in the region 250–400 kNm was about 1.194 E+08 Nm/rad. This number reflects the combined torsional stiffness of elements numbered 1 through 4 (Figure 2) (the motor, torque limiter, and flexible high-speed coupling, the dynamometer gearbox). The calculated combined torsional stiffness $\left(\frac{1}{K_M}+\frac{1}{K_{HS-C}}+\frac{1}{K_{tl}}+\frac{1}{K_{DGB}}\right)$ from the values listed in Table 1 is 2.84 E+08 Nm/rad. Despite the uncertainty in the test data, slope approximation in measurements leads to a good agreement in the order of magnitude of the stiffness obtained from calculations. This also validated the dynamic torsional equivalence of the gearbox model used in the stiffness calculations (Appendix A).

3.4 Model Reduction and Torsional Mode Sensitivities

Given that the torque measurements were available on the LSS side of the dynamometer, the three-mass model was useful to establish and identify the most dominant torsional mode within 4.8% difference from experimental measurements. If measurements were also available at additional locations along the torque load path, several other possibilities for modelling and element grouping exist that may lead to similar conclusions. In the following, a few reduced order models are presented together with the discussion on their accuracy in representing the torsional modes.

3.4.1 Two Mass Spring-Damper Model of the Dynamometer

If the gearbox inertia can be ignored, a reduced order model with a two-mass spring damper system can be realized.

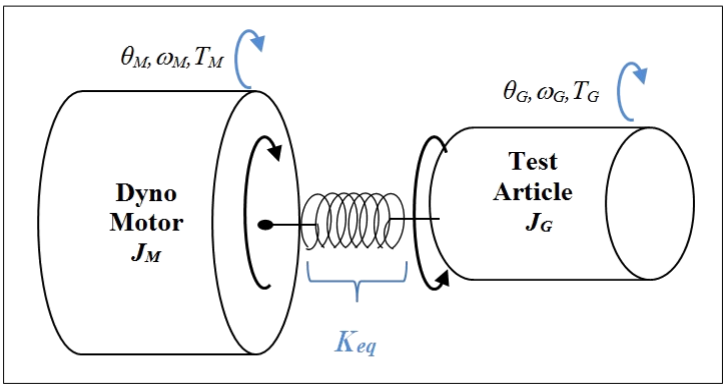

Figure 8. Two-mass equivalent of the 2.5-MW dynamometer

Under such case, the torsional vibrations can be determined using the dynamics equations for two-degrees of freedom [12]:

$$\begin{bmatrix} \dot{\omega_M} \\ \dot{\omega_G} \\ \dot{\theta_M} \\ \dot{\theta_G} \end{bmatrix} = \begin{bmatrix} -B_M/J_M & 0 & -K_{eq}/J_M & K_{eq}/J_M \\ 0 & -B_G/J_G & K_{eq}/J_G & -K_{eq}/J_G \\ 1 & 0 & 0 & 0 \\ 0 & 1 & 0 & 0 \end{bmatrix} \begin{bmatrix} \omega_M \\ \omega_G \\ \theta_M \\ \theta_G \end{bmatrix} + \begin{bmatrix} 1 & 0 \\ 0 & -1 \\ 0 & 0 \\ 0 & 0 \end{bmatrix} \begin{bmatrix} T_M \\ T_G \end{bmatrix} \tag{7}$$

where B_M and K_{eq} represent the damping and stiffness lumped between the dynamometer motor and the test article equivalents. The dynamometer and test article speed and angle are in the directions as defined in Figure 8. Considering free vibration in an undamped system where B→0, the normal mode solution for these linear differential equations assumes a second order polynomial with two modes and natural frequencies given by:

$$\begin{bmatrix} \omega_1 \\ \omega_2 \end{bmatrix} = \begin{bmatrix} 0 \\ \sqrt{\frac{(J_M+J_G)}{J_M \times J_G} \times K_{eq}} \end{bmatrix} \tag{8}$$

The value of the equivalent stiffness in the model depends on the compliance contributed by elements from the test article and the dynamometer. Figure 9 shows the dynamometer elements considered for each study case. Table 3 lists the modal frequencies obtained by accounting and discounting some stiffness and inertia in the system.

In all of the cases, the first mode represents the rigid body mode, while the second mode results in a condition where the dynamometer motor and the test article are out of phase with each other. The mode shape for one such case is shown in Table 4. The second mode still results in frequencies that are close to the 6.2 Hz measured during experiments.

Table 3. Frequencies and Mode Shapes (Two-Mass Model)

Mode	Frequency
1	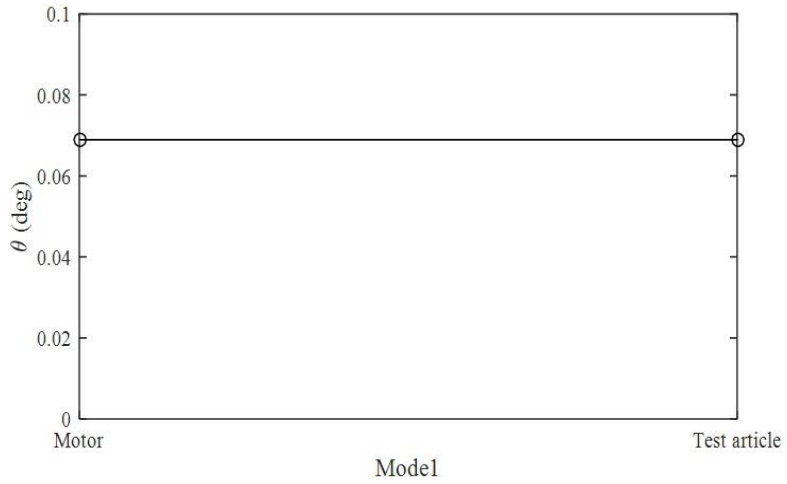
2	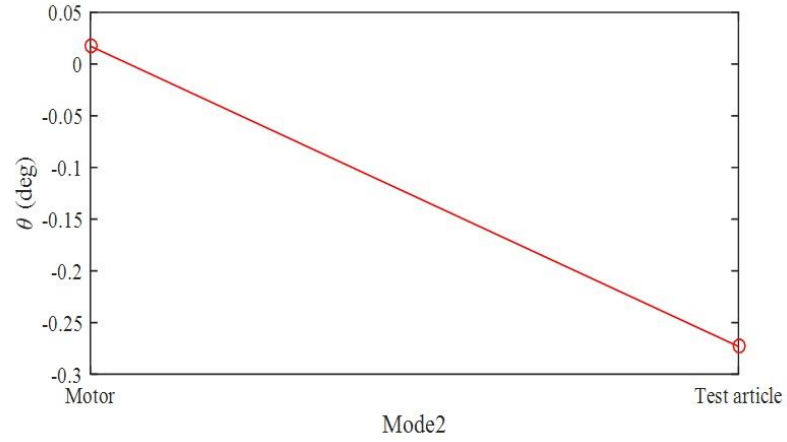

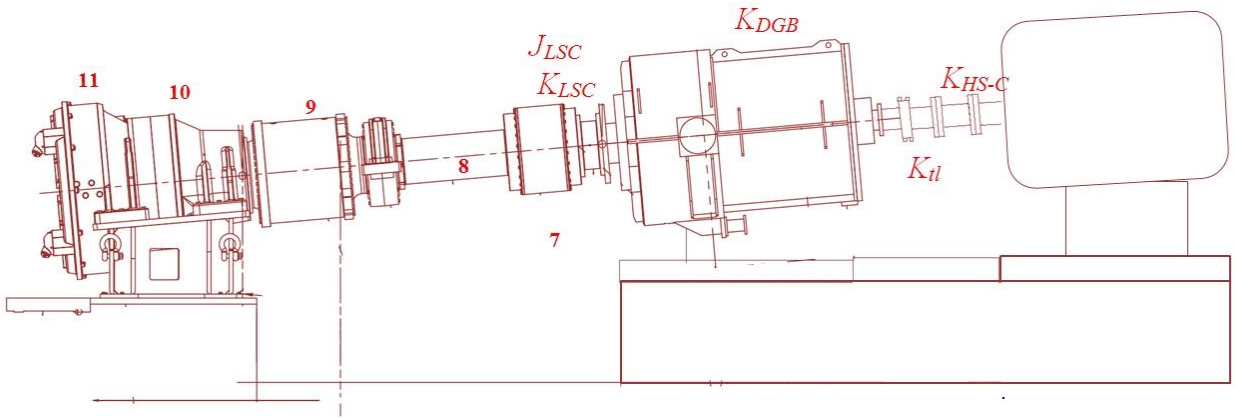

Figure 9. Dynamometer elements considered for each study case. ***Illustration reproduced from [5]***

Table 4. Two-Mass Spring Damper System: Sensitivity Case Studies

Cases	K_{DGB}	J_{LSC}	J_{TA}	$J_{HS-C}+J_{tl}$	K_{eq}	J_G	Mode	Frequency
Case 1	✘	✘	✘	✘	$\frac{1}{K_{eq}}=\frac{1}{K_M}+\frac{1}{K_G}$	$J_G= J_{Gen}$	1	0 Hz
							2	6.5507 Hz
Case 2	✘	✓	✓	✘	$\frac{1}{K_{eq}}=\frac{1}{K_M}+\frac{1}{K_G}$	$J_G= J_{Gen}+J_{TA*}$	1	0 Hz
							2	6.24 Hz
Case 3	✓	✘	✘	✘	$\frac{1}{K_{eq}}=\frac{1}{K_M}+\frac{1}{K_{DGB}}+\frac{1}{K_G}$	$J_G= J_{Gen}$	1	0 Hz
							2	6.2558 Hz
Case 4	✓	✓	✓	✘	$\frac{1}{K_{eq}}=\frac{1}{K_M}+\frac{1}{K_{DGB}}+\frac{1}{K_G}$	$J_G= J_{Gen}+ J_{TA*}$	1	0 Hz
							2	5.96Hz
Case 5	✓	✓	✓	✓	$\frac{1}{K_{eq}}=\frac{1}{K_M}+\frac{1}{K_{DGB}}+\frac{1}{K_G}$	$J_M= J_M + J_{HSC}+J_{TL}$	1	0 Hz
							2	5.96Hz

TA constitutes items 7 through 10*

3.4.2 One Mass-Spring Damper System

With an inertia that is at least 15.7 times greater than that of the test article, the dynamometer motor behaves as an immovable object. At the same time, the equivalent torsional stiffness of the test article (the next-generation drivetrain) was found to be at least one order of magnitude smaller than that of the dynamometer; hence, the compliance in the torque path was dominated by the test article. As compared to the gearbox and the motor, the torque limiter appears to be a weaker element. Hence, it may also be possible to simplify the two-mass model to a single-mass spring damper system considering the inertia of the test article drivetrain. The stiffness elements in the torque path include all those elements beginning from the low speed coupling of the dynamometer (Figure 10).

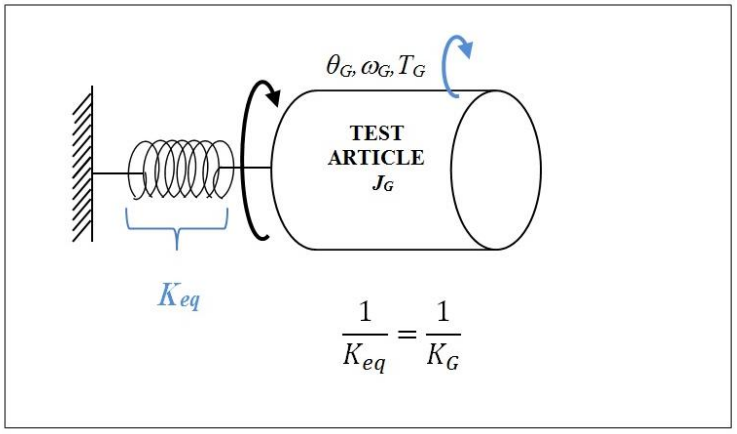

Figure 10. One-mass damper model of the dynamometer

$$T_G = K_{eq}\theta_G + J_G\dot{\omega}_G \; and \; \omega = \sqrt{\frac{K_{eq}}{J_G}} \tag{9}$$

The natural frequency computed using the simplified torsional vibration equation (9) for an undamped system with one degree of freedom is 6.8 Hz. If the inertia of the test article is also included, then the frequency reduces to 6.5 Hz.

In summary, all three model representations are able to capture the significant torsional mode within 10%. The torsional description using the three-mass model was most useful to establish the phase relationship between dynamometer gearbox and the test article drivetrain. A more inclusive grouping of element inertia and stiffness can lead to more complex dynamometer main shaft modes. Although it may be possible to capture the higher excitation frequencies (namely, 42.01 Hz, 62 Hz, and 92 Hz) using higher model fidelity and higher degrees of freedom, such an exercise was not necessary in the present context.

3.4.3 Sensitivities to Test Article Properties

The present modelling and measurement campaign identified 6.1 Hz as the fundamental torsional mode of the 2.5-MW dynamometer and current next-generation drivetrain test article. This frequency depends on the rating and size of the test article; in general, larger test articles tend to lower frequencies as the dynamometer becomes a more dominant driver of compliance.

In the case of the next-generation drivetrain, the ratio of the inertias of the dynamometer motor and the test article (J_G/J_M) was 0.063. This ratio for a majority of commercially available wind turbines ranging from 1 MW to 2.5 MW is $0.04 \leq J_G/J_M \leq 0.1$ [12]. The stiffness ratio (K_G/K_M) for the drivetrain was 0.155. The exact values and the relationship between the torsional stiffness and rotational inertia of commercial turbines are indeterminate at this stage, yet it is evident that both inertia and stiffness drive the natural frequencies. Hence, if the test article was replaced with a drivetrain characterized by a higher stiffness or inertia, then the fundamental torsional vibration modes are likely to change. The sensitivities of the torsional modes to different combinations of test article torsional characteristics were tested considering the three-mass model presented in Section 3.

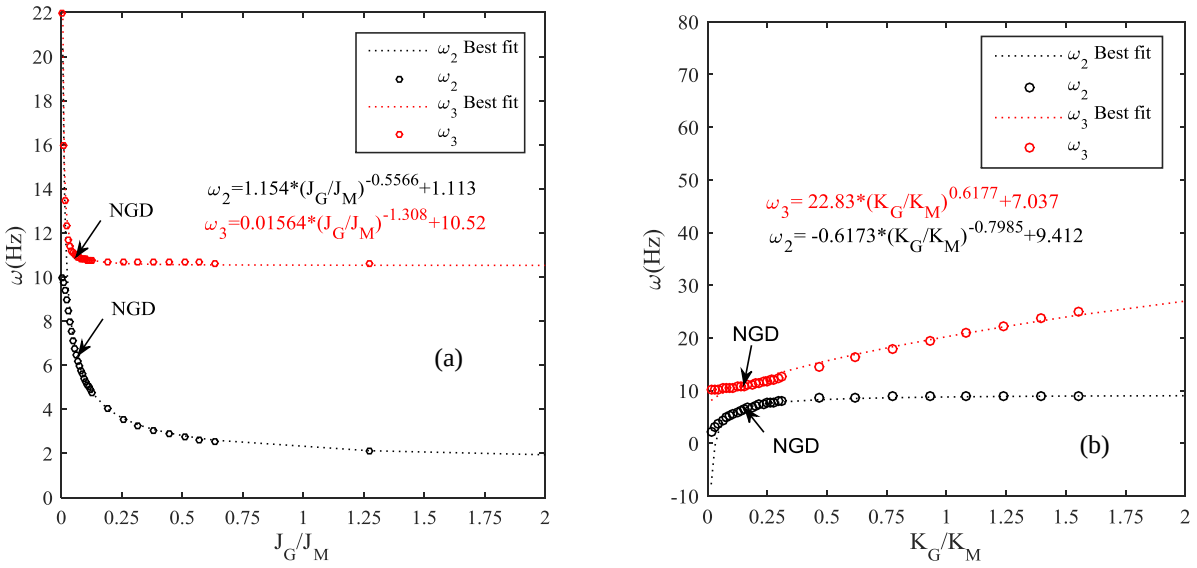

Figure 11. Torsional mode sensitivity: (a) Test article inertia, (b) Test article stiffness

Referring to Figure 11, hypothetically, if the test article has a higher inertia but has comparable stiffness properties as compared to the next-generation drivetrain, then the fundamental torsional vibration mode (ω_2) is expected to be reduced. When the inertia of the test article becomes comparable to the dynamometer motor, i.e., if J_G/J_M is unity, then the torsional resonance can be expected at frequencies as low as 1.5 to 2 Hz whereas a much lighter test article is expected to drive up the frequencies.

A stiffer test article with inertia similar to that of the next-generation drivetrain increases the excitation frequencies. When the stiffness is comparable to that of the dynamometer, i.e., if

K_G/K_M is unity (the stiffness is at least 6 times that of the next-generation drivetrain), the most significant vibration mode (ω_2) increases to 8.9 Hz. If the inertia and stiffness represented by the test article are as big as that of the dynamometer motor, then about 9% reduction can be expected for ω_2. As the test article becomes substantially heavier and stiffer than the dynamometer motor, the torsional mode would be dictated by compliance in the dynamometer side.

4 Damping

The most significant torsional mode identified in the earlier discussions requires active damping for safe and successful operation of the dynamometer. Section 3 demonstrated the extent of the torsional oscillations introduced by this high-energy mode and the relative increase in decay response time at power levels higher than 200kNm. A high decay response time implies that the energy trapped in the vibration takes longer to dissipate because of low damping. Possible causes may include (1) lightly damped characteristics of the dynamometer gearbox resulting in low damping when coupled to a high power generator or as in the case of the next-generation drivetrain's permanent-magnet generator; (2) the sensitivities of electromechanical torque characteristics to disturbance frequencies that are within the generator's voltage regulation bandwidth, which can be counterproductive to the net effective damping in the overall mechanical drivetrain. Although mechanical damping may be used to offset the poor damping characteristics, mechanical damping requires additional hardware and mechanical components that can increase the weight and cost of a system. The optimal control objective to mitigate the torsional excitation in the dynamometer becomes one of increasing the damping in the system. In the model development, the damped and undamped natural frequencies were assumed to be very similar; hence, a deliberate exclusion of damping term was preferred as it complicates mathematical expressions for eigenfrequencies. The equation for the undamped oscillation is expressed using:

$$x = Ce^{-\delta\omega_n t}\cos(\omega t) \qquad (10)$$

where C represents the amplitude of oscillation, δ the damping ratio, and ω_n the natural frequency.

An estimate on damping ratios estimated from low-speed torque measurements at two different power levels is shown in Figure 12.

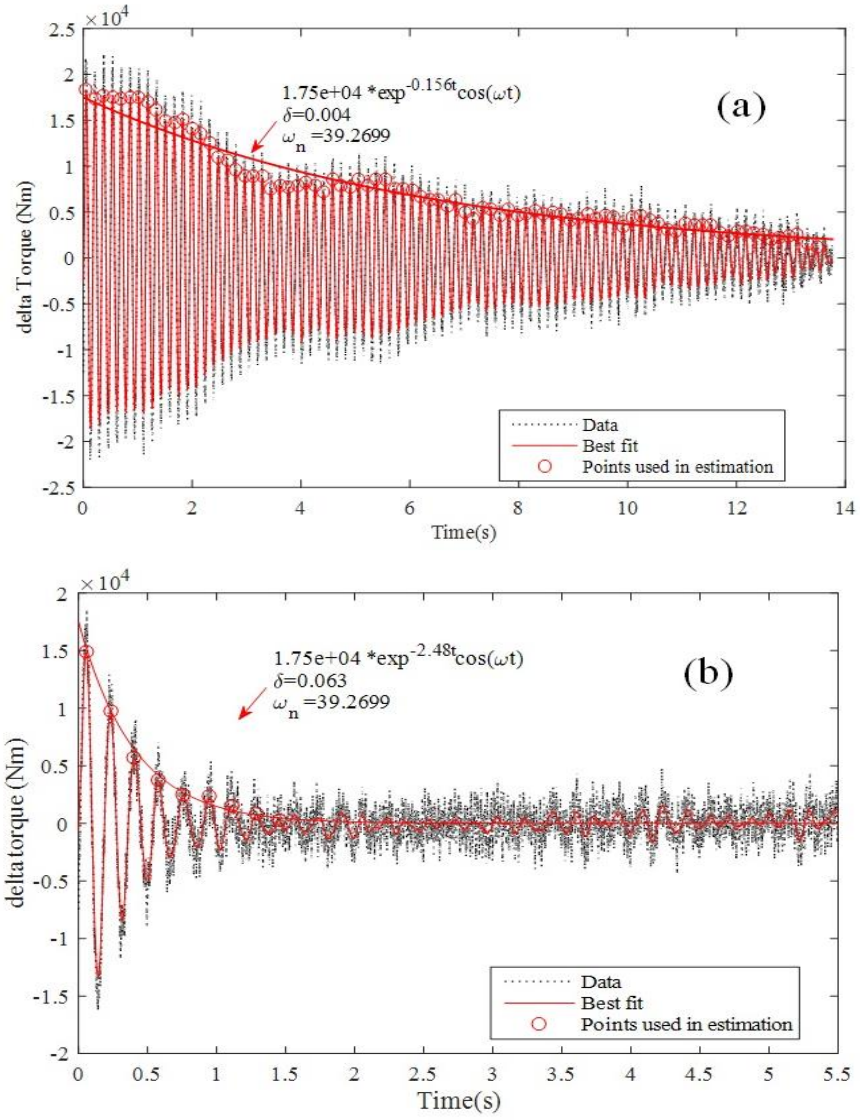

Figure 12. Damping estimated from low-speed torque measurements at different power levels: (a) 220 kNm, (b) 50 kNm

These correspond to average torque levels of 220 kNm and 50 kNm, respectively. As may be observed, approximately 6.3% damping was present at lower torque compared to just 0.4% at a higher torque. Two approaches to compensate for the torque oscillations were investigated and implemented.

4.1 Electrical Damping

In the first approach, we attempted to damp the torsional oscillations by increasing the resistance of electric load damper that formed the RC filter circuit on the DC bus. The existing connection of load bank comprised of resistors connected in series (Figure 13) forming a net equivalent resistance of 50 Ω. These resistor banks were rewired to decrease the resistance to 11.26 Ω. The intention was to selectively increase the electrical resonant frequency above the bandwidth of mechanical resonant frequency.

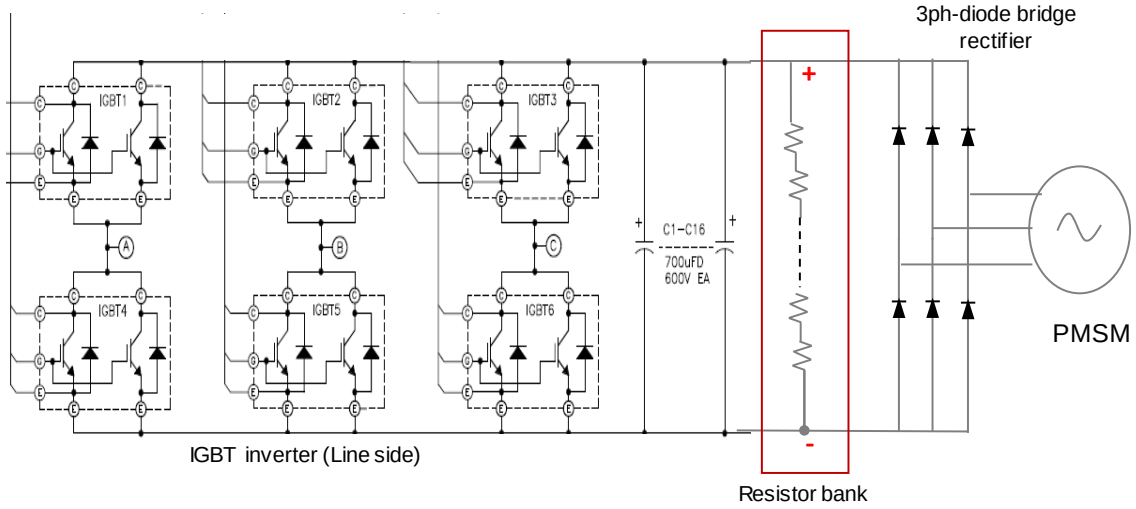

Figure 13. Pulse width modulation inverter-diode bridge rectifier circuit. *Illustration reproduced from [13]*

Figure 14 shows the estimated damping ratios at higher and lower torque levels. At similar power levels as the uncompensated system discussed earlier, no significant improvement was observed to be achieved by this method.

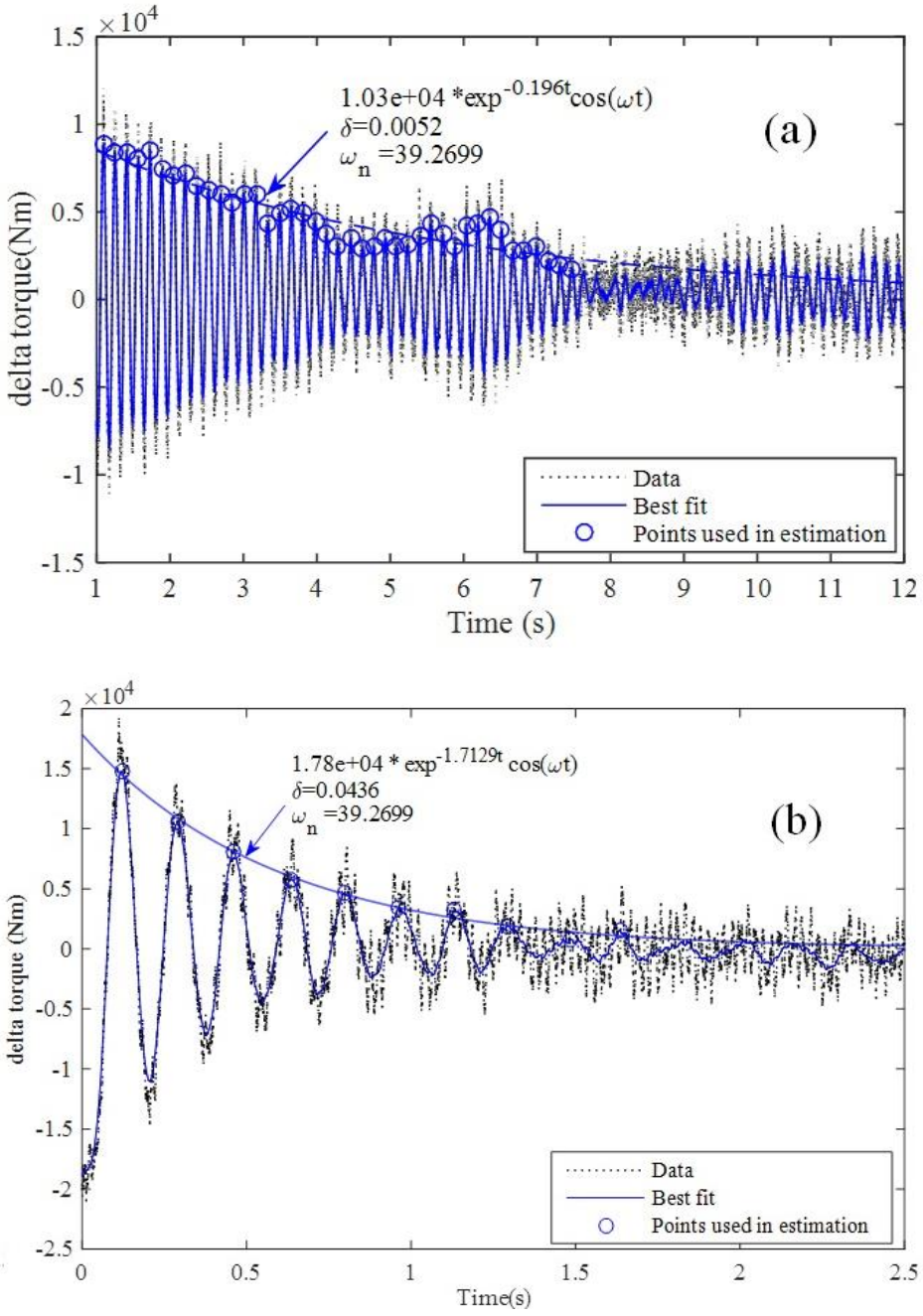

Figure 14. Mechanical damping achieved by electrical damping: (a) 220 kNm, (b) 70 kNm

4.2 Compensation Tuning

The dynamometer motor is powered by a variable frequency ACS2000 drive [14] that implements a direct-torque flux control algorithm. This method consists of first estimating a reference stator flux and electromagnetic torque through speed control. The estimated stator flux and electric torque are then controlled directly by comparing them with their respective demanded values using current and voltage measurements by means of hysteresis modulation.

In the speed control mode of the dynamometer motor, a certain set point speed is commanded of the variable frequency drive. An encoder measures the instantaneous speed on the high-speed shaft and the signal is low-pass filtered and fed back into a speed control loop that is proportional-integral error regulated. A speed ramp rate controls the time taken by the motor to accelerate and decelerate. The values for the proportional and integral gains are 10 and 2.5, respectively. The output of the controller is a torque set point (with an upper and lower saturation limit of +/-20 kNm) that feeds into the direct-torque flux control block for controlling the torque.

In an attempt to damp the torque oscillations, compensation tuning was provided by a feedforward speed command signal. The compensation filtered the measured dynamometer torque on the low-speed shaft (T_{LSS}) with a first-order Butterworth bandpass filter. A bandwidth of 4–9 Hz was deliberately chosen to filter the dominant 6-Hz content in the torque signal. The filtered torque signal was then multiplied by a gain term, G_{LSS}, of 0.012 and then added to the speed command for the dynamometer motor as shown in the block diagram. The intention of this tuning was to derive the 6-Hz content from the torque signal and feedback to the reference speed command, by scaling the torque signal on the LSS because no speed measurement was made in that part of the drivetrain.

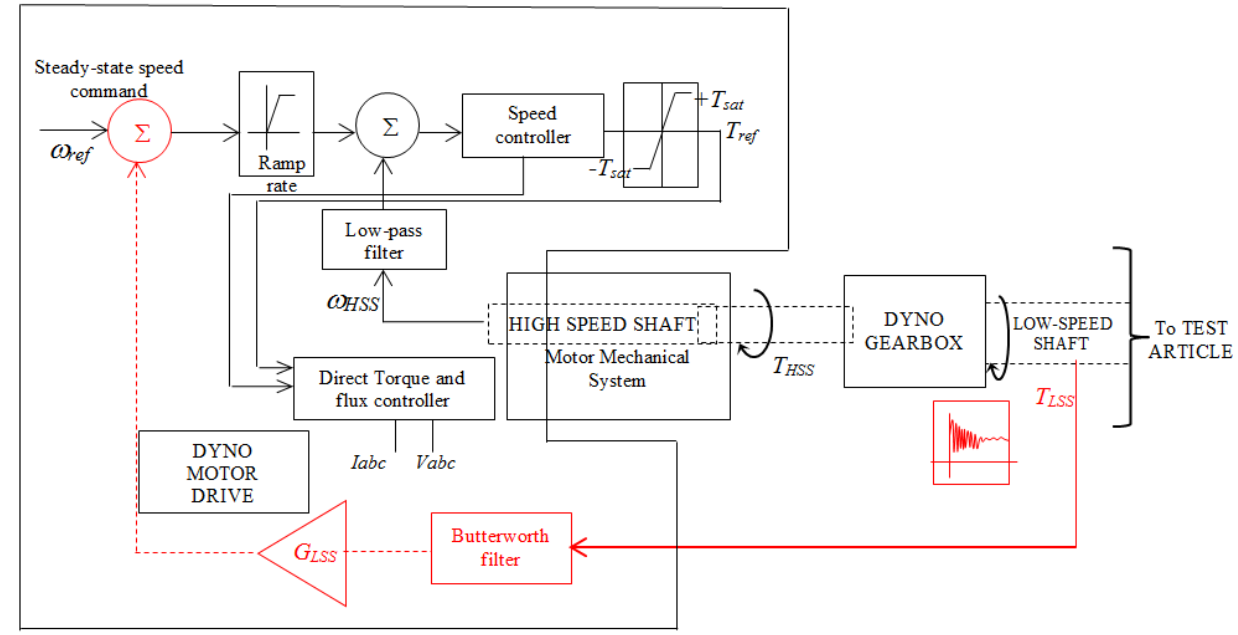

Figure 15. Speed control architecture in the dynamometer (objects shown in red correspond to compensation tuning)

As may be observed from Figure 16 (a), this approach yielded a considerably higher damping, averaging about 12% at 220 kNm. A comparison of damping (Figure 16 [b]) achieved by the two approaches discussed so far against the uncompensated system showed that compensation tuning was a more effective approach, especially at higher power levels.

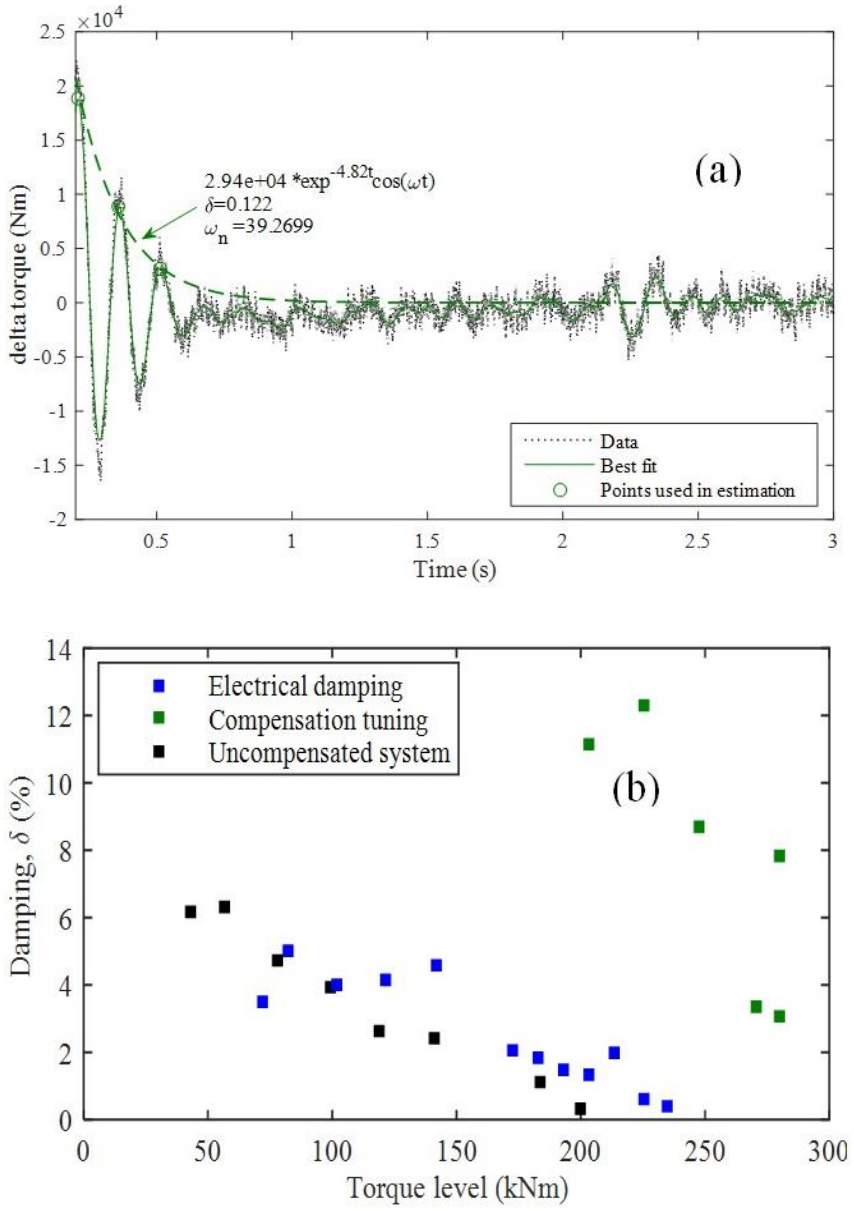

Figure 16. (a) Damping achieved by compensation tuning; (b) comparison of the two damping approaches at different power levels

4.3 Simulink Model

To examine the damping compensation approach more closely, a Simulink model of the dynamometer test article was created. This model was built using MATLAB's SimPowerSystems and SimDriveline toolboxes that provide component libraries and analysis tools for modeling, designing, and simulating electrical, mechanical, and control systems. The main advantage of such tools is the availability of a single simulation environment that enables testing the performance of the complete system by combining dynamics from different elements.

SimDriveline is particularly useful for analyzing a one-dimensional mechanical system and supporting rotational and translational components, such as gears and clutches that can be used to model mechanical power transmission. Because torque transmission is the main focus of the present study, this tool is relevant and provides the required level of fidelity and the flexibility to include certain effects (e.g., meshing and viscous losses) and balances the tradeoff between model fidelity and simulation time.

The basic block diagram of the Simulink model is shown in Figure 17. The model consists of three basic blocks, namely, the dynamometer motor block; the mechanical and the power block, which emulates a combination of speed control; and the power control capability of the dynamometer.

The dynamometer motor block is a simplified representation of the dynamometer induction motor drive unit that emulates the speed and torque control for a certain speed set point. The motor is characterized by an ideal torque source that is actuated by a proportional integral controller. The output of the proportional-integral controller is a torque set point (a Simulink signal) that saturated at ±20 kNm. The K_P and K_I gains for the controller are 100 and 0.04, respectively. A low-pass filter (LPF) with a frequency of 200 Hz ensured an optimal bandwidth suitable for speed loop. The torque source is a mechanical element that accepts a physical signal as input. A Simulink-Physical signal (S-PS) block converts the Simulink signal to a physical signal compatible with the torque source.

The mechanical block begins from the output of the torque source. The mechanical elements are interconnected by physical signals (shown by yellow lines) that transmit speed/torque. The inertia of the motor is represented as an ideal rotational inertia ($T = Jd\omega/dt$) attached to a reference point. The torque is positive if the inertia is accelerated in the positive direction and vice versa. A flexible shaft represented by a spring-damper system was used to represent the high-speed, low-speed, and generator shaft (torque tube). A simple gear block was used to model the dynamometer gearbox and the test article gearbox that constrains the two connected driveline axes, base (B) and follower (F), to co-rotate at a fixed ratio of 51.3832 and 0.17, respectively. About 3% loss in power was assumed from meshing losses. Inertia 2 represents that of the dynamometer gearbox. Sensors measure the speed and torque in the high-speed, low-speed, and generator shafts.

The power block includes the electromagnetic power circuit model of the drivetrain and a simplified representation of the converter. The test article generator is modeled using the permanent-magnet synchronous machine block available from the Simulink library. The block accepts torque input from the mechanical block through rotational mechanical port (S). The model assumes a linear magnetic circuit with no saturation of the stator and rotor iron. The

generator speed is determined from its inertia and the difference between the applied mechanical torque and internal electromagnetic torque T_e.

The existing power converter configuration in the dynamometer with the next-generation drivetrain is of voltage source type [15]. The grid side has a pulse width modulation (PWM)-controlled two-level insulated gate bipolar transistor converter with gating signals generated by space vector modulation. A power circuit regulates current and the PWM scheme such that the generator's electromagnetic torque results in a certain desired active power output. The power converter's DC link is fed from the rectified output of the generator. Because there were no detailed parameters for the various circuit elements available, we decided to mimic this system using a simplistic controller. The output of the PMSM block feeds into a three-phase PWM diode rectifier block and current source regulated by a proportional integral (PI) controller. At each instant the power flowing in the DC bus (computed from the voltage across the DC bus and the current) feeds into the PI loop that generates the current set point to minimize the error between the desired and measured power output. The output of the PI controller is low-pass filtered before it is used to actuate the current source.

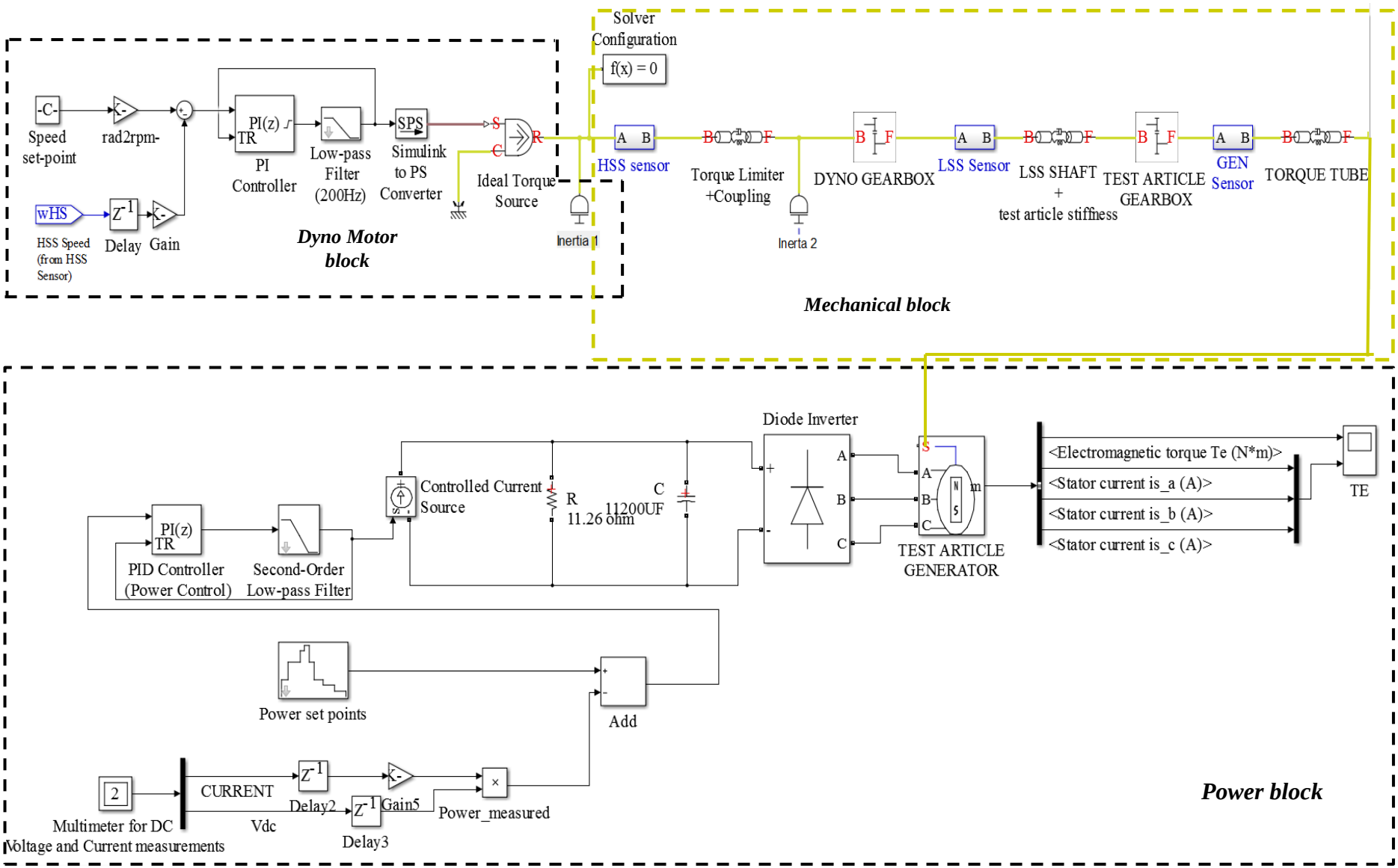

Figure 17. Simulink model of the dynamometer with the next-generation drivetrain

4.3.1 Model Validation

Two different cases are presented to demonstrate the reproducibility of test conditions using the model. Case 1 presents the validation of modeling results against measured data, whereas Case 2 presents only the modeling results.

4.3.1.1 Case 1

In Case 1, the torque responses to a series of load step increments were simulated. This process consisted of progressively increasing the power demand from 19 kW to 220 kW followed by a step-wise reversion.

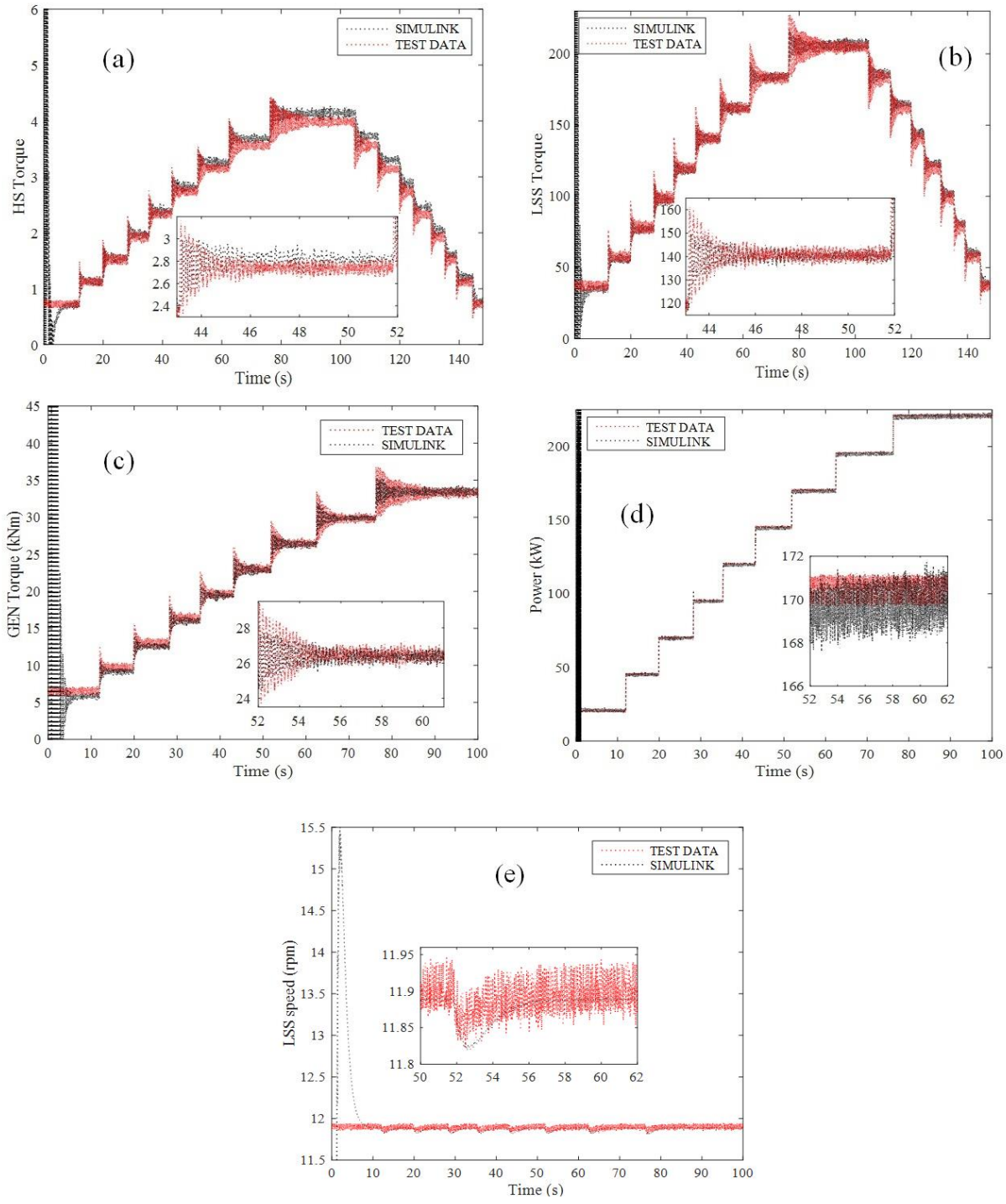

Figure 18. Model versus test data: (a) – (c) Torque measurements, (d) Power, (e) LSS speed

Figure 18 shows a comparison of time series for power, torque signals from the three sensors, and LSS speed against test data. The value of K_P and K_I gains of the power control circuit were tuned (at 0.08 and 0.08, respectively) to achieve a reasonable agreement in power. It may be observed from these plots that the amplitudes of the oscillations are higher compared to the

response predicted by Simulink, and a slight offset in mean torque exists in the high-speed section. The subplots featuring the time histories between 40 and 60 seconds show a phase lag between the model and test data. This was expected since delay blocks in the sensor measurements were not synchronized to match with the latency observed in the test data. (No attempt was made to simulate the resolution of the measurement devices used in testing). The comparison of torque frequency spectra (Figure 19) show the 6-Hz content in the simulation, with the test data showing higher energy content around this peak.

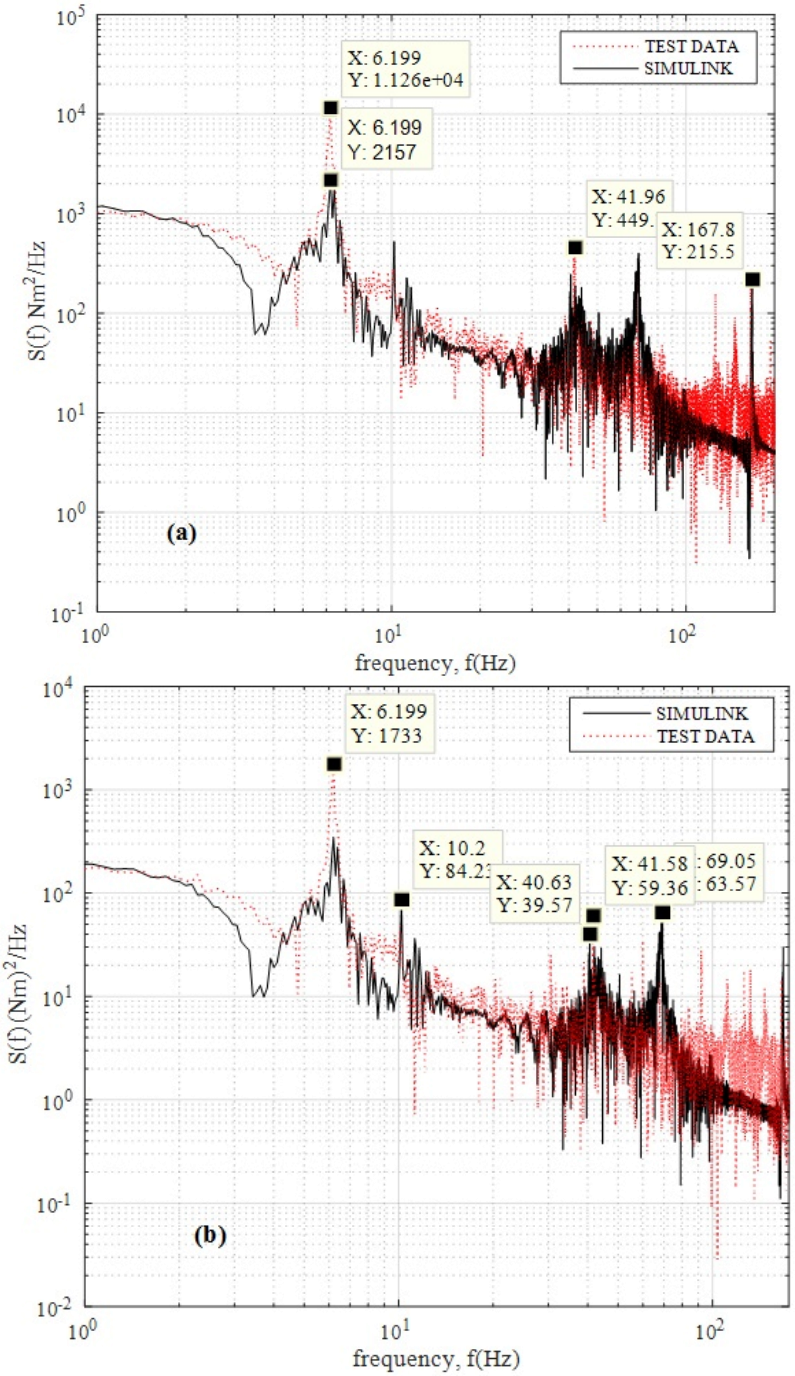

Figure 19. Comparison of frequency spectra: (a) LSS torque, and (b) generator torque

Apart from the second fundamental frequency (10.2 Hz), additional harmonics (between 40 Hz and 70 Hz) are also identified by the model; these are expected to be caused by electrical resonant frequency as also permitted by the LPF bandwidth in the power control circuit.

The comparison of speeds on the LSS was made with reference to the motor speed referred to the LSS side (because the speed measurements were only made on the dynamometer motor). The PI regulator on the speed control loop was found to reasonably track the reference speed and respond to step changes in power. Hence, no further tuning was necessary.

4.3.1.2 Case 2

Case 2 simulates the test condition in which the torque oscillations grew in size and became unstable at higher power levels (above 220 kW). Torque levels on the LSS were progressively increased from 75 kNm to 300 kNm while maintaining an average speed of 11.9 rpm. As may be observed in the power plot, the oscillations tend to become unstable at 250kW and begin to grow in size beyond 250kW. The same is reflected in the torque measurements on the high-speed shaft and the LSS as well as the generator (Figure 20). The frequency of these oscillations was 6.39 Hz.

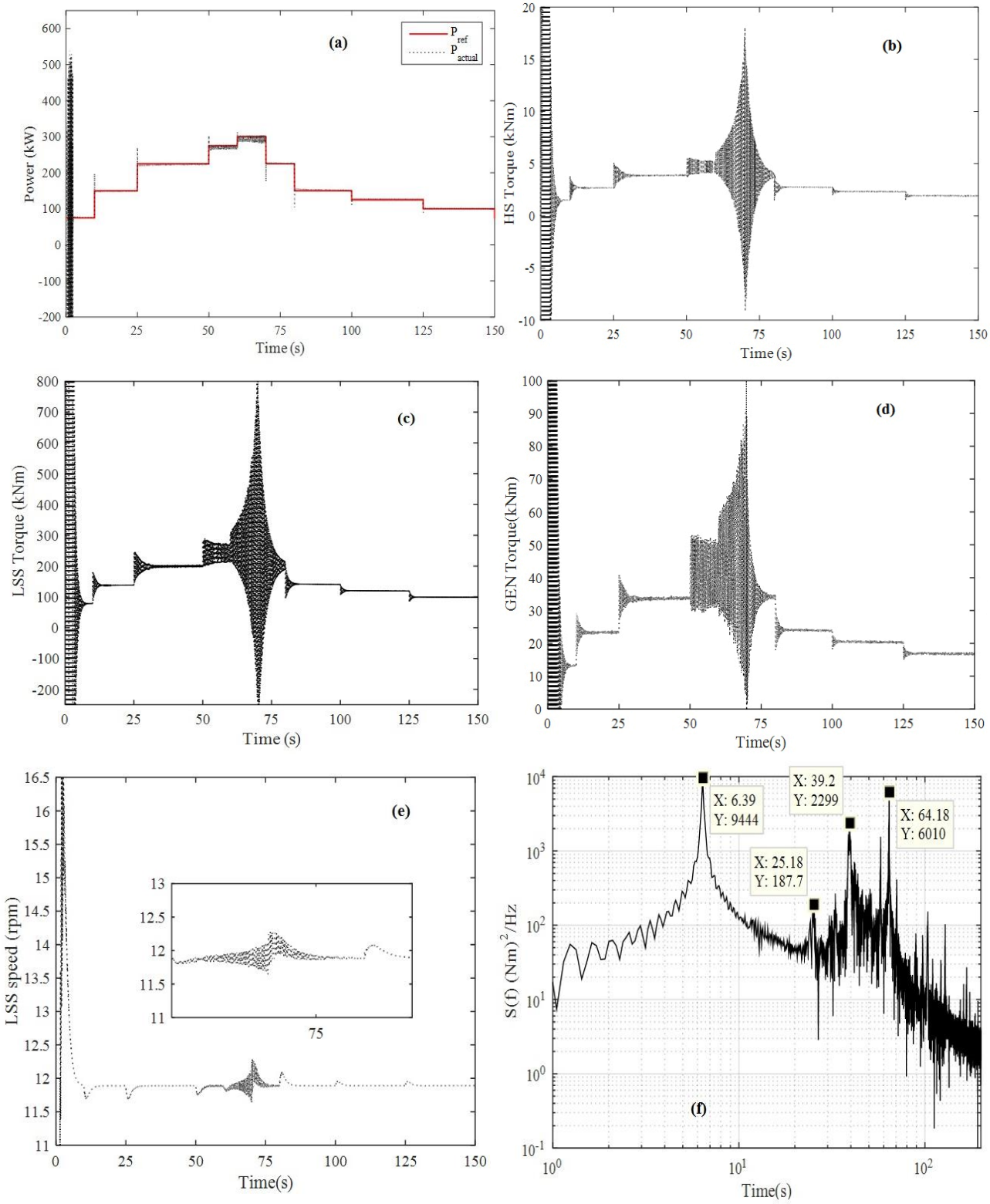

Figure 20. (a) Power demanded vs. controller output; (b–d) torque measurements at the high-speed, low-speed, and generator shafts; (e) LSS speed; and (f) frequency spectra of generator torque

4.3.2 Torque Sensitivities to Power Control Parameters

Approaches to damp the torque oscillations were tested with the Simulink model. In the first approach, the LPF upper cut-off frequency ($f_{cut\text{-}off}$) in the power control circuit was tuned to examine the sensitivities of torque response. Figure 21 shows a comparison of the generator

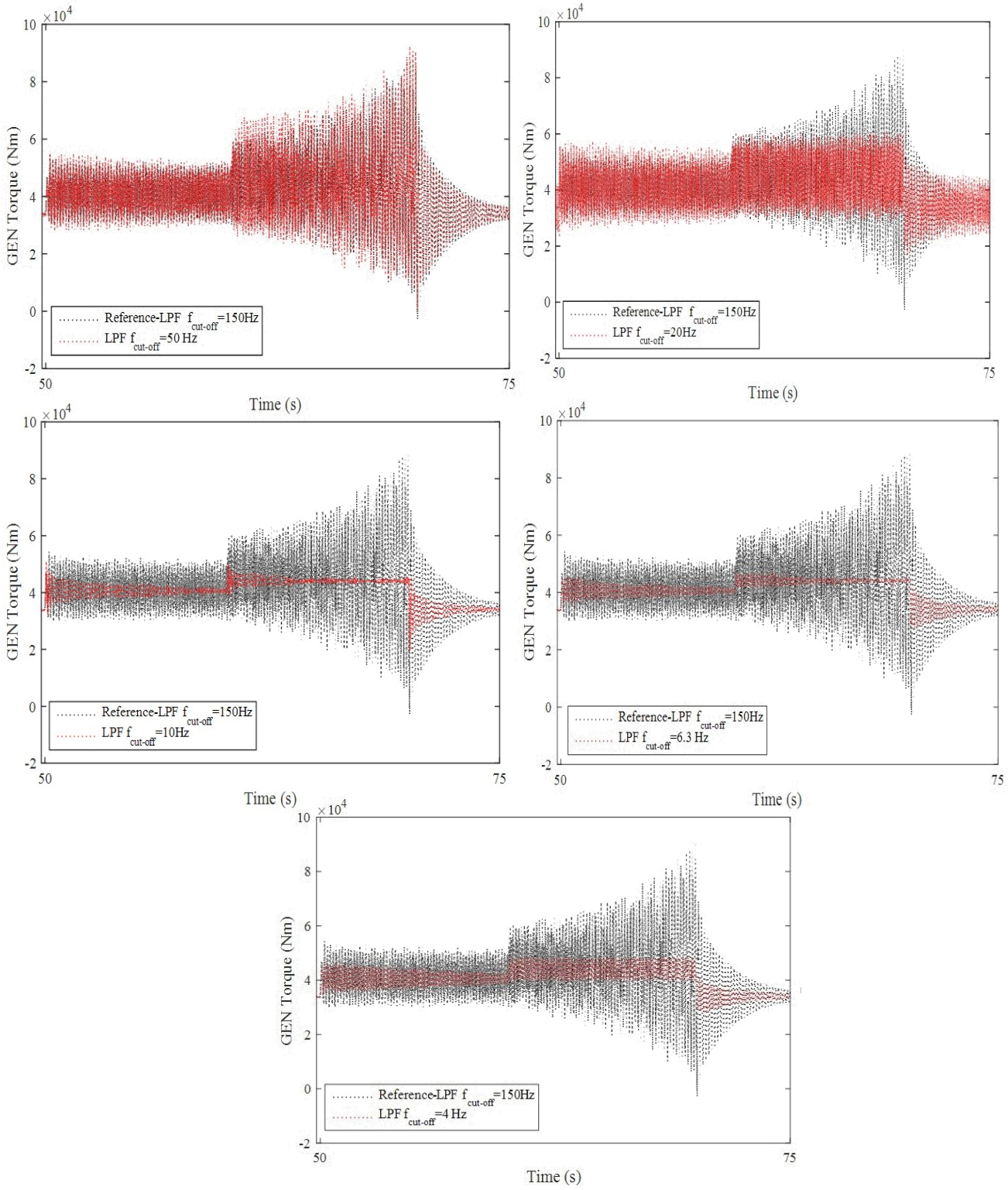

Figure 21. Generator torque oscillations at different LPF cut-off frequencies

torque at higher power levels in the unstable region (for the reference case discussed in Case 2) against the tuned cases. The value of $f_{cut\text{-}off}$ in the reference model was 150 Hz. This was reduced to a much smaller range (6-50Hz) to examine the possibility of avoiding the 6-Hz excitation. The torque oscillations are smallest when $f_{cut\text{-}off}$ is below 10 Hz and above 4 Hz. Thus, the optimal filter bandwidth was found to lie between 4 and 10 Hz.

In the second approach, a band-stop (notch) filter was added in series with the LPF in the power control circuit. This was found to have the effect of reducing the oscillations, but required the tuning of the LPF filter to notice an appreciable improvement. As may be inferred from generator torque oscillations (Figure 22), the addition of a notch filter does not help significantly improve the response unless the LPF $f_{cut\text{-}off}$ is also tuned to 10 Hz. Thus, it is reasonable to conclude that the output of the LPF filter dictates the nature of torque response.

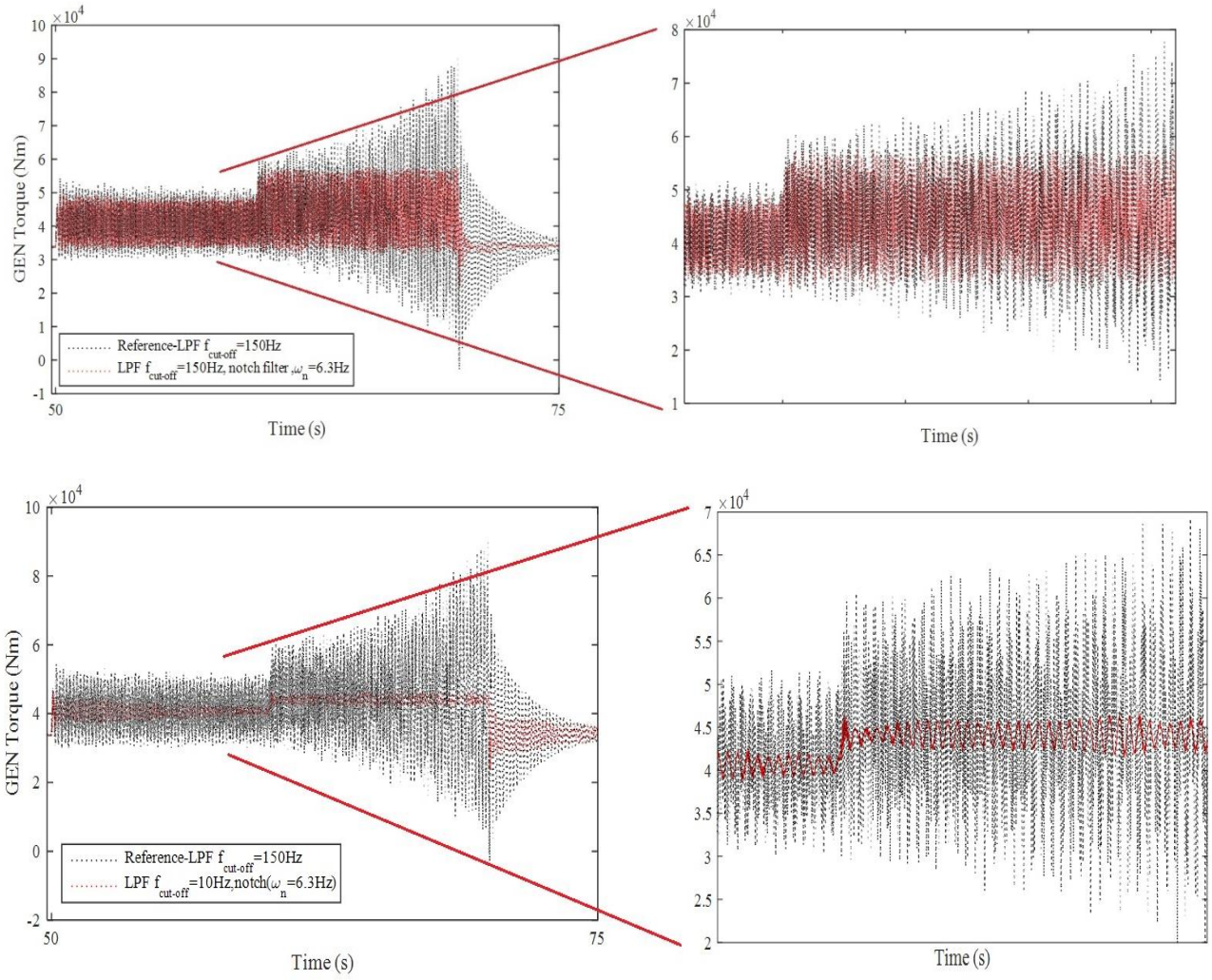

Figure 22. Generator torque oscillations after inclusion of notch filter

In the third sensitivity study, compensation tuning discussed in the previous section was implemented in the Simulink model. The value of K_{LSS} was varied between 1% and 4% of the original value of 0.012. Figure 22 shows substantial reduction in oscillations at 4%. The reduction may be attributed to a possible introduction of additional damping from the torque feedback, such that the compensation behaves as a damping controller. Referring to a similar technique described in [16] and considering a one-mass-spring damper system, the equation of motion in torsion is given by

$$T = J_{eq}\ddot{\theta} + B_{eq}\dot{\theta} + K_{eq}\theta \tag{11}$$

It is suspected that if the torque feedback augments the existing speed control loop, intuitively an additional damping term of the form $T_{LSS}K_{LSS} \longrightarrow B_{LSS}\dot{\theta}$ is introduced.

Applying the new damping term in equation (12) and taking the Laplace transform results in

$$J_{eq}s^2 + (B_{eq} + B_{LSS})s + K_{eq} = 0, \tag{12}$$

which can be re-written to give

$$s^2 + 2\zeta\omega s + \omega^2 = 0 \tag{13}$$

where, ω is the natural frequency in torsion and the new damping ratio, is given by

$$\zeta = \frac{B_{eq}+B_{LSS}}{2J_{eq}\omega} \tag{14}$$

It is emphasized that no effort was made to tune the delay blocks to account for phase lag between the model and measurements. Further work shall account for delays introduced by measurements from analog circuitry that was present during testing can help minimize the phase lag between the model predictions and measurements.

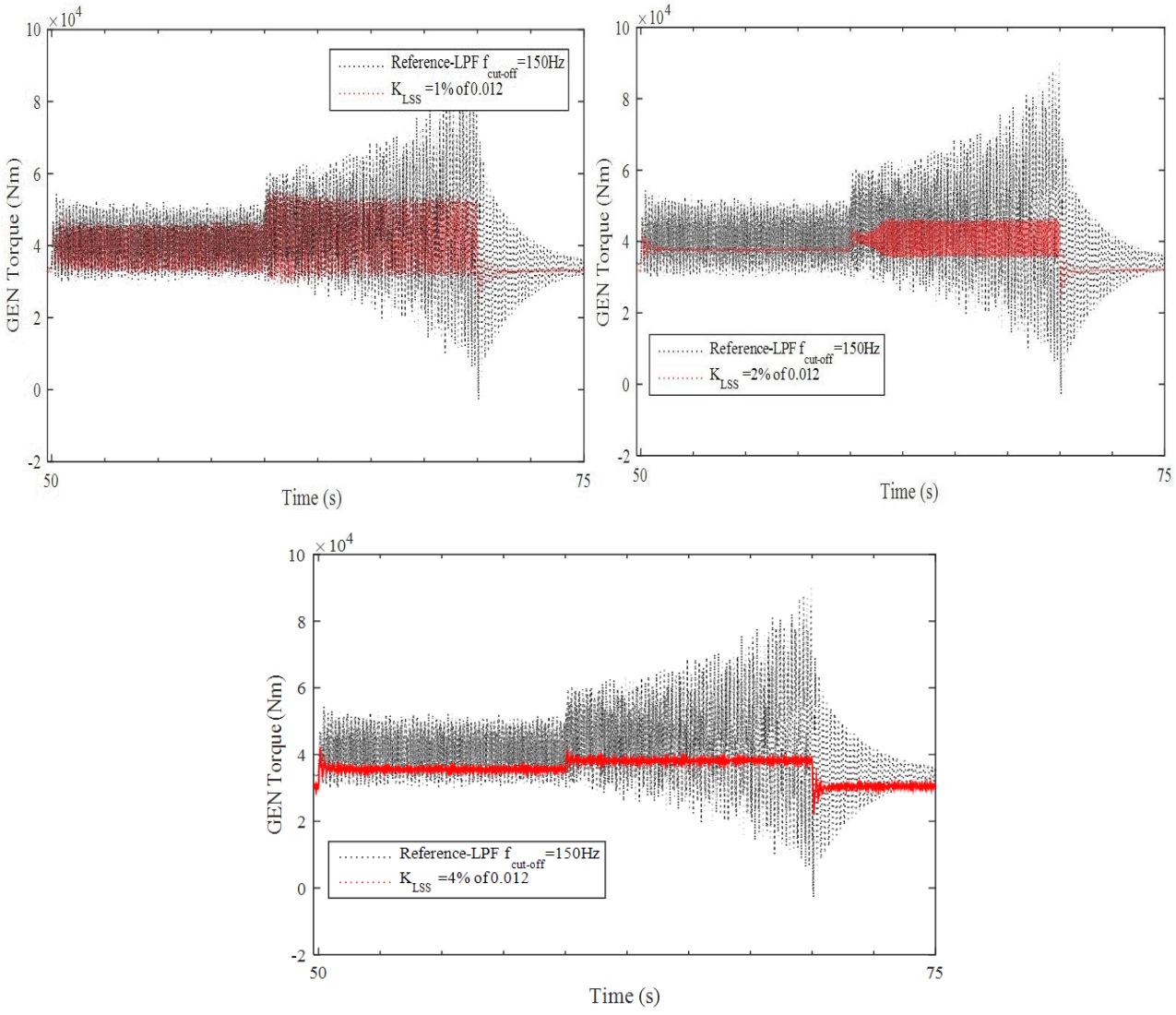

Figure 23. Generator torque oscillations after compensation tuning

5 Conclusions

The fundamental torsional mode of the dynamometer with the next-generation drivetrain was experimentally identified as 6.1 Hz, with torque oscillations at the low speed shaft and generator shaft being in phase with each other. Detailed derivations for the torsional modes using lumped parameter models concur with this observation. The lumped parameter three-mass model was found to be the most convenient to capture the eigenmodes and the mode shapes that resembled the phase relationship between the LSS and the generator torques observed during testing. The detailed list of stiffness and inertia parameters is documented in the Appendices for future reference.

The location of the torsional modes depends on the rating, size of the test article, and visco-elastic properties. In general, larger test articles tend to lower the eigenfrequencies as the dynamometer becomes a more dominant driver of compliance. Simple analytical tools to forecast these frequencies were presented. The sources for large torque oscillations are expected to be due to a combination of lightly damped characteristics of the dynamometer gearbox and the sensitivities of electromechanical torque characteristics to disturbance frequencies that are within the generator's power regulation bandwidth.

Two approaches, electrical damping and feedforward speed compensation, were studied to reduce the oscillation induced by the torsional resonances at 6.1Hz. The experimental data suggested substantial improvements in system damping with the latter. To examine damping more closely, a simplified Simulink model emulating the dynamics of the electrical, mechanical, and control system of the dynamometer and test article was created using MATLAB's Simpowersystems and SimDriveline tools. Both speed and power regulations are implemented using simplified PI controllers. Torque responses at the high-speed, low-speed, and generator shafts were validated for a step change in power between 19 kW and 200 kW. An approximate 90° phase lag existed between the model and the test data. This was due to the unsynchronized delay blocks that needed to be included to account for latency that was present at the time of the measurements. The simulations also showed instability at a higher power level (300 kW). The extent of the oscillations was found to be most sensitive to LPF bandwidth in the power control circuit. Feedforward compensation of the dynamometer motor reference speed using a low-speed torque signal was found to be a promising approach and substantially damped the torque response; it is expected that the torque feedback acts as a damping controller that augments the existing speed controller to damp the torsional oscillations in the system. Thus, the model provides initial guidance on tuning the various control parameters that may be required to circumvent potential excitation under torque testing of the dynamometer.

References

National Renewable Energy Laboratory. "Dynamometer Test Facilities." Last updated: November 11, 2013. http://www.nrel.gov/wind/facilities_dynamometer.html

Keller, J., B. Erdman, D. Blodgett, C. Halse, and D. Grider. "Next Generation Drivetrain Development and Test Program." Paper presented at the Conference for Wind Power Drives, November 30 – December 2 2015, Bremen, Germany, http://www.nrel.gov/docs/fy16osti/65497.pdf, Accessed February 2016.

W. Erdman. "Control and correlation of main shaft torsional modes on wind turbines and off-axis loaded dynamometers," Torsional Vibration Symposium, Salsburg 2014.

National Renewable Energy Laboratory. (Undated). http://www.nrel.gov/wind/pdfs/nwtc_dynamometer_specifications.pdf, Accessed December 2015.

Voith Torque Limiting Couplings, SafeSet, SmartSet and AutoSet, http://voith.com/de/1831_e_cr421en.pdf. Accessed December 2015.

Ameridrives flexible coupling, C-220 assembly drawing: DWG-MB-220265. Internal document (Undated).

Amerigear Gear Couplings Standard and Modified Designs. http://www.gmbassociates.co.uk/downloads/Amerigear%20Standard%20Couplings%20Catalogue.pdf, Accessed December 2015.

Powertrain Engineers Inc. GEC Load test layout drawing: 0202-10227-80.Rev 4. Internal document (Undated).

Rockwell Automation. Rotor data for torsional calculations, NREL e-mail communication, 1998.

Rexroth flexible coupling Series 52- Mass elastic data. Internal communication (Undated).

Philadelphia Corporation. Gearing Specifications: Mass elastic data for MOD2 modified test stand. NREL e-mail communication, May 1999.

Modelling, Control and Simulation of Torsional Dynamics of Drivetrain, Romax Report, internal document, March 31, 2015. 1552-DC-006-A.

BEW Engineering. Schematic system, main power/control 510kVA photovoltaic inverter. Internal document (Undated).

"ACS2000. Flexible and reliable: technology leading medium voltage drivers for a wide variety of applications. "Accessed January 2016. http://new.abb.com/drives/medium-voltage-ac-drives/acs2000.

Douglas C. Blodgett, Michael R. Behnke, and William L. Erdman. "Power converter control algorithm design and simulation for the NREL next generation drivetrain," DNV KEMA Renewables, internal only, September 30, 2014.

Darrow, J., K. Johnson, A. Wright. 2011. "Design of a tower and drive train damping controller for the three-bladed controls advanced research turbine operating in design-driving load cases," *Wind Energy*, Vol 14, Issue 4, Pages 571–601. DOI: 10.1002/we.443.

Appendix A. Gearbox Equivalent Stiffness Calculation

The layout and the main components of the gearbox are available in [8]. The torsional dynamic equivalent of the dynamometer gearbox was formulated such that its analogous equations of motion produce the same output response for a given input as the original system (Figure A-1). The total kinetic energy and the strain energy stored in the original system and the equivalent system are identical. The equivalent spring stiffness is the reciprocal of sum of the reciprocal stiffnesses of individual springs referred to the low-speed side, while the equivalent inertia was the sum of the inertia of referred to the low-speed side.

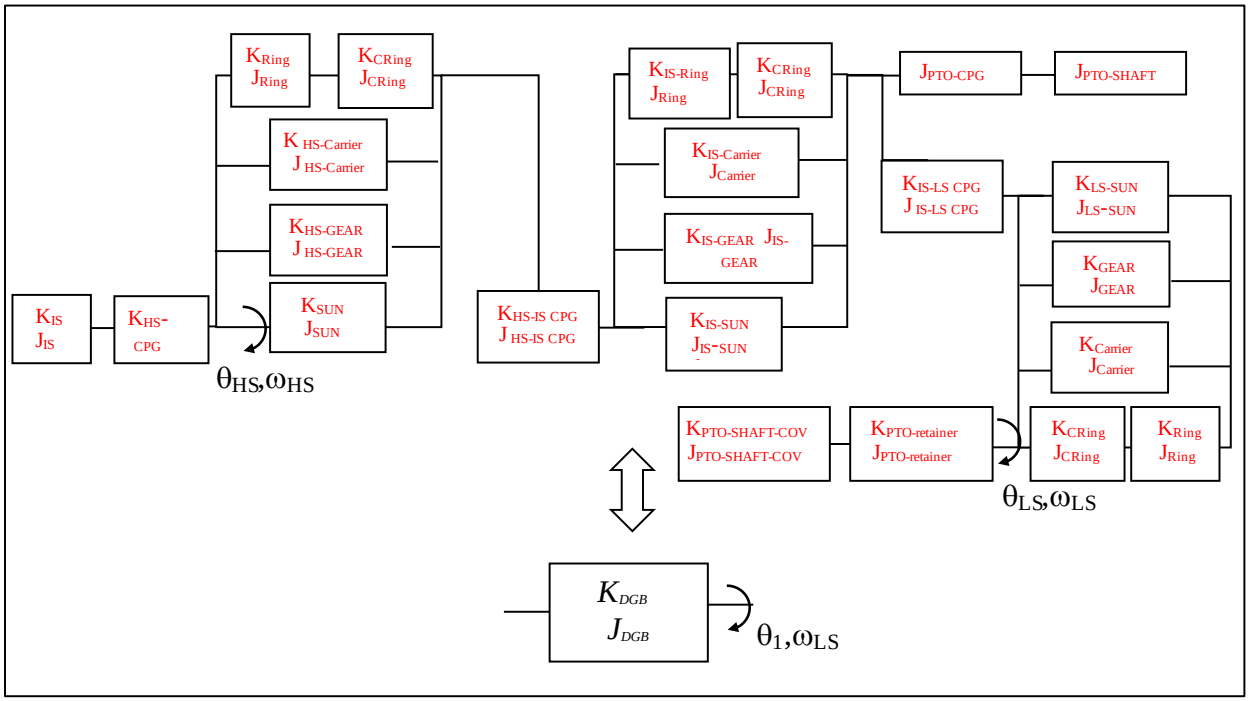

Figure A-1. Torsional dynamic equivalent of the dynamometer gearbox

$$\text{Total strain energy: } P.E = \frac{1}{2}\left(\frac{1}{n_1^2}\left(\frac{1}{K_{IS}}+\frac{1}{K_{CPG}}+\frac{1}{K_{SUN}}\right)+\frac{1}{n_2^2K_{HS-GEAR}}+\frac{1}{n_3^2K_{HS-Carrier}}+\frac{1}{n_4^2}\left(\frac{1}{K_{HS-Ring}}+\frac{1}{K_{HS-IS\,CPG}}+\frac{1}{K_{HS-IS\,CPG}}\right)+\frac{1}{n_5^2K_{IS-Carrier}}+\frac{1}{n_7^2}\left(\frac{1}{K_{IS-Ring}}+\frac{1}{K_{IS-CRing}}+\frac{1}{K_{IS-LS\,CPG}}+\frac{1}{K_{LS-SUN}}\right)+\frac{1}{n_9^2}\left(\frac{1}{K_{LS-Carrier}}+\frac{1}{K_{LS-Spindle}}+\frac{1}{K_{LS-PTO}}+\frac{1}{K_{LS-PTO-SHAFT}}\right)+\frac{1}{n_{10}^2K_{LS-CRing}}\right)\theta_1^2$$

$$Total\ Kinetic\ energy, K.E$$
$$= \left(n_1^2(J_{IS} + J_{CPG} + J_{SUN}) + n_2^2 J_{HS-GEAR} + n_3^2 J_{HS-Carrier}\right.$$
$$+ n_4^2\left(J_{HS-Ring} + J_{HS-CRing} + J_{HS-IS\,CPG} + J_{HS-SUN}\right) + n_5^2 J_{IS-Carrier}$$
$$+ n_6^2 J_{IS-PGear} + n_7^2\left(J_{IS-Ring} + J_{IS-CRing} + J_{IS-LS\,CPG} + J_{LS-SUN} + J_{LS-SUN}\right)$$
$$+ n_8^2 J_{LS-GEAR} + n_9^2(J_{LS-GEAR} + J_{LS-Carrier} + J_{LS-Spindle} + J_{LS-PTO}$$
$$\left. + J_{LS-PTO-SHAFT}\right)\theta_1^2$$

The main components identified from the gearbox manufacturer's data sheet are listed in Table A-1. The respective component inertia and stiffnesses referred to their own speeds and to the low-speed shaft are provided for reference.

Table A-1. Main Components Identified from the Gearbox Manufacturer's Data Sheet

Item No.	Component	Symbol	Moment of Inertia Self (kg-m^2)	Symbol	Torsional Stiffness (Nm/rad)	Speed ratio	Moment of Inertia LS-side (kg-m^2)	Torsional Stiffness LS-side (Nm/rad)
1	Input Shaft	I_{IS}	2	K_{IS}	2.06E+09	n_1	5,680	5.43E+12
2	HS Spline Coupling	I_{HS-CPG}	-	K_{HS-CPG}	1.29E+07	n_1	488	3.39E+10
3	HS Sun pinion	I_{HS-SUN}	2	K_{HS-SUN}	1E+07	n_1	4,607	2.65E+10
4	HS Planet Gear	$I_{HS-GEAR}$	6	$K_{HS-GEAR}$		n_2	13,347	4.46E+10
5	HS Carrier	$I_{HS-Carrier}$		$K_{HS-Carrier}$	2.90E+08	n_3		
6	HS Annulus Gear	$I_{HS-Ring}$	138	$K_{HS-Ring}$	-	n_4	36,493	-
7	HS Inner coupling Ring HS Outer Coupling Ring	$K_{HS-CRing}$	60	$K_{HS-CRing}$	2.74E+10	n_4	16,135	7.32E+12
9	HS/IS Spline Coupling	$I_{HS-IS\,CPG}$	187	$K_{HS-IS\,CPG}$	6.68E+08	n_4	50,021	1.79E+11
10	IS Sun Pinion	$I_{IS\,SUN}$	1	$K_{IS\,SUN}$	4.76E+07	n_4	343	1.27E+10
11	IS Planet Gear	$I_{IS\,PLANETS}$	39	-	-	n_5	2,889	-
12	IS Carrier	$I_{IS\,Carrier}$	-	$K_{IS\,Carrier}$	9.41E+08	n_6	-	7.21E+09
13	IS Annulus Gear	$I_{IS-Ring}$	343	$K_{HS-Ring}$	-	n_7	3,814	-

Item No.	Component	Symbol	Moment of Inertia Self (kg-m^2)	Symbol	Torsional Stiffness (Nm/rad)	Speed ratio	Moment of Inertia LS-side (kg-m^2)	Torsional Stiffness LS-side (Nm/rad)
14	IS Inner Coupling Ring IS Outer Coupling Ring	$I_{IS-CRing}$	134	$K_{IS-CRing}$	3.23E+10	n_7	1,485	3.58E+11
15	IS/LS Spline Coupling	$I_{IS-LS\ CPG}$	432	$K_{IS-LS\ CPG}$	2.03E+08	n_7	4,805	2.26E+09
16	PTO Coupling	$I_{PTO-CPG}$	5	$K_{PTO-CPG}$	-	n_7	56	-
17	PTO Coupling Shaft	$I_{PTO-CPG-SHAFT}$	8	$K_{PTO-CPG-SHAFT}$	-	n_7	92	-
18	LS Sun Pinion	$I_{IS\ SUN}$	36	$K_{IS\ SUN}$	1.44E+10	n_7	402	1.6E+11
19	LS Planet Gear	$I_{LS\ PGEAR}$	551	-	-	n_8	7,220	-
20	LS Planet Gear	$I_{LS\ PGEAR}$	427	-	-	n_9	427	-
21	LS Planet Carrier, Output Shaft	$I_{LS\ Carrier}$	1646	$K_{LS\ Carrier}$	1.55E+09	n_9	1,646	1.55E+09
22	LS Spindle	$I_{LS\ Spindle}$	217	$K_{LS\ Spindle}$	-	n_9	217	-
23	LS Annulus Inner Coupling Ring LS Outer Coupling Ring	$I_{LS-CRing}$	-	$K_{LS-CRing}$	1.24E+10	n_{10}	-	2.10E+10
24	PTO Outboard Bearing Retainer	I_{LS-PTO}	1	-	-	n_9	1	-
25	PTO Shaft Cover	$I_{LS-PTO-SHAFT}$	1	-	-	n_9	1	-
Total inertia of the gearbox referred to LS side					J_{DGB}	n_9	150619	
Total rotational stiffness of the gearbox referred to LS side					K_{DGB}	n_9	6.87E+08	

Appendix B. Test Article Equivalent Stiffness Calculation

The dynamometer is connected to the main shaft of the next-generation drivetrain test article through the low-speed coupling. An adapter and carrier shaft complete the torque path to a single-stage planetary gearbox. The output shaft of the gearbox is connected to the generator rotor through a torque tube. The dynamic equivalent of the test article was obtained by transforming the respective component inertias and stiffnesses to the low-speed side using the same principle discussed for the gearbox. The components of the test article originally identified in Figure 2 (from 7 through 11) are laid out as shown in Figure B-1. The mechanical properties are listed in Table B-2. Figure B-2 shows the element grouping used in computing the equivalent properties

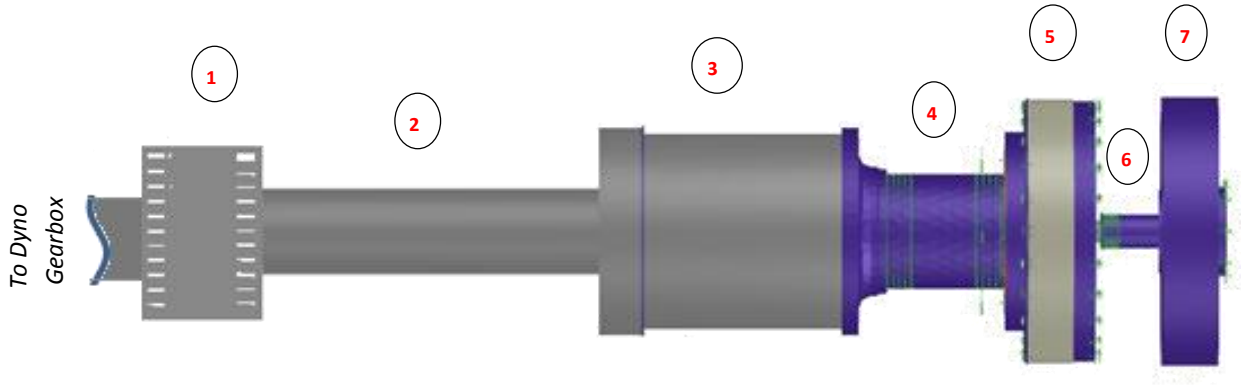

Figure B-1. Test article assembly. ***Illustration reproduced from [12]***

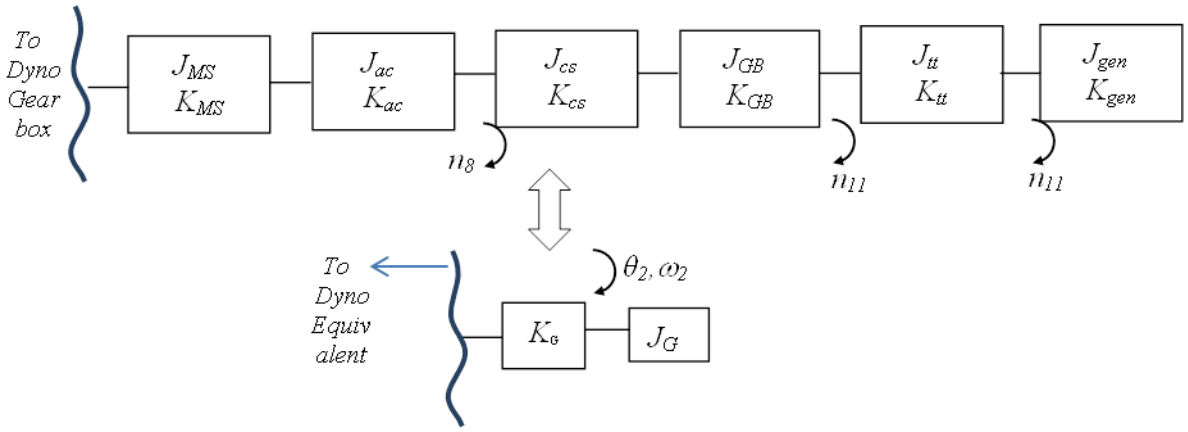

Figure B-2. Torsional dynamic equivalent of the test article

$$\frac{1}{K_G} = \frac{1}{n_8^2 K_{MS}} + \frac{1}{n_8^2 K_{ac}} + \frac{1}{n_8^2 K_{Gb}} + \frac{1}{n_{11}^2 K_{tt}}$$

$$J_G = n_8^2 J_{MS} + n_8^2 J_{ac} + n_8^2 J_{Gb} + n_{11}^2 J_{gen}$$

$$J_G = n_8^2 J_{MS} + n_8^2 J_{ac} + n_8^2 J_{Gb} + n_{11}^2 J_{gen}$$

where n_8 =1, n_{11} =5.82

Table B-2. Mechanical Properties of Test Article

Item No.	Component	Symbol	Moment of Inertia Self (kg-m^2)	Symbol	Torsional Stiffness (Nm/rad)	Speed ratio	Moment of Inertia LS-side (kg-m^2)	Torsional Stiffness LS-side (Nm/rad)
1	Low-Speed Coupling	J_{LSC}	656	K_{LSC}	1.2E+10	n_8	656	1.2E+10
2	Main Shaft	J_{MS}	533	K_{MS}	3.35E+08	n_8	533	3.35E+08
3	Adapter Can	J_{ac}	1,616	K_{ac}	9.67E+09	n_8	1,616	9.67E+09
4	Carrier Shaft	J_{cs}	-	K_{cs}	-	n_8	-	-
5	Gearbox	J_{GB}	1,540[a]	K_{GB}	1.19E+08[b]	n_8	1,540	1.19E+08
6	Torque Tube	J_{tt}	4	K_{tt}	1.89E+07	n_{11}	135	6.36E+08
7	Generator Rotor	J_G	1,230	K_{gen}	-	n_{11}	41663	-
Total inertia referred to low-speed side (kg-m^2)						J_{TA}	46144	
Total torsional stiffness referred to low-speed side (Nm/rad)						K_G	7.6E+07	

[a] The inertia includes that of the carrier shaft (3)

[b] The computed stiffness values includes that of the carrier shaft (3), planetary ring-gear set (4), and the generator (5) with the relevant speed ratios accounted for.

The combined torsional stiffness of the next-generation drivetrain gearbox and the generator was computed from the RomaxWIND model [11]. Torque in steps of 50 kNm was applied to the carrier shaft at the low-speed end and the torsional twist was measured. The slope was 1E+08 Nm/rad (Figure B-3).

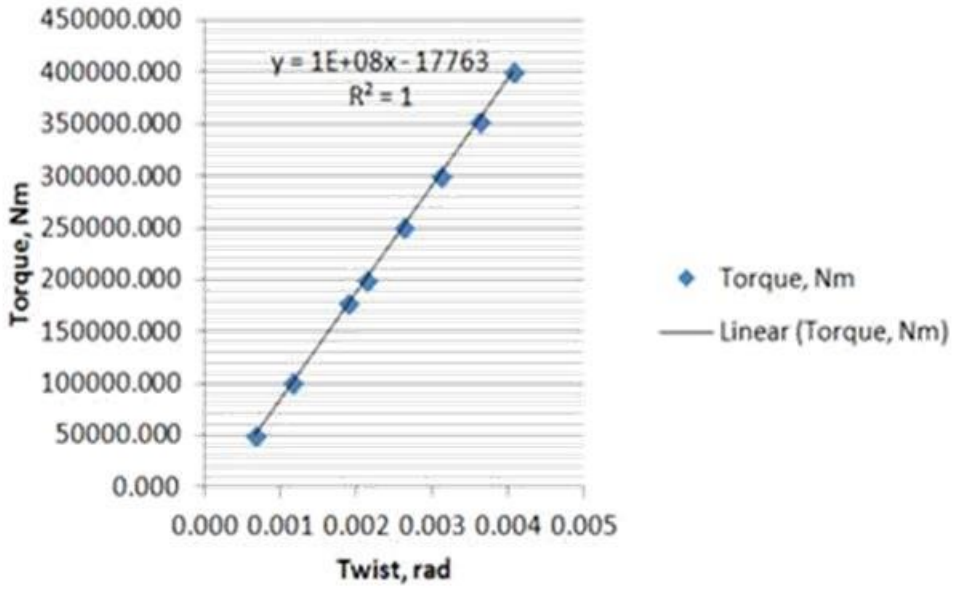

Figure B-3. Combined torsional stiffness of the next-generation drivetrain gearbox and the generator computed from the RomaxWIND model